

Constructing an External Cavity Diode Laser for the Probing of Rydberg Excitons in Cu₂O

by

Aaron Gross

A thesis
presented to the University of Waterloo
in fulfillment of the
thesis requirement for the degree of
Master of Science
in
Electrical and Computer Engineering

Waterloo, Ontario, Canada, 2021

© Aaron Gross 2021

Author's Declaration

I hereby declare that I am the sole author of this thesis. This is a true copy of the thesis, including any required final revisions, as accepted by my examiners.

I understand that my thesis may be made electronically available to the public.

Abstract

Cuprous oxide (Cu_2O) is a direct bandgap semiconductor that presents a promising platform for the implementation of a solid state quantum simulator. This promise is in part due to the presence of excitons in the material which have the potential to become excited to Rydberg states, which are robust even in the presence of liquid nitrogen temperature thermal environments. The properties of the Rydberg excitons in Cu_2O can be studied by the proxy of a series of P-exciton resonance peaks. For the study of peaks corresponding to principle quantum number $n > 12$ in the yellow P-series, high resolution spectroscopy methods are required due to the n^{-3} scaling of the width of each resonant peak. However, a tunable narrow linewidth light source, such as an external cavity diode laser, can be used to resolve these states by scanning the wavelength of the laser and measuring its transmission through a sample. Such a laser source can also be used in further experiments to probe and manipulate the excitonic state of the material, by for example inducing a Rydberg blockade.

A narrow line-width tunable laser system capable of generating the required wavelengths of light via cavity enhanced second harmonic generation to scan the yellow P-exciton spectrum is constructed, and a high resolution transmission scan is performed. The results of the scan show close agreement with previously and concurrently obtained white light transmission spectroscopy results. This close agreement is somewhat corroborated by further qualitative analysis performed by fitting an asymmetric Lorentzian function to visible exciton resonance spectral features, and comparing the extracted values of the function parameters between the white light and laser light data.

Acknowledgements

I would like to begin by thanking the members of my thesis committee, my advisor Prof. Na Young Kim, as well as Prof. Kyung Soo Choi and Prof. Dayan Ban, for taking the time to read my thesis and provide their feedback and insight. I would also like to thank Prof. Kim in her capacity as my advisor for helping me to navigate my graduate experience by providing support and feedback, as well as fostering a sense of curiosity and an appreciation for the beauty inherent in the mechanics of our world.

The work I did on this project was supported by many others, and I would like to thank each of them in turn. First, I would like to begin by thanking Dr. Daniel Kang, from whom I inherited this project, for the foundational work he did in designing and building several components of the project, as well as for his mentorship and guidance both the practical and theoretical aspects of the project.

I would like to thank Marcel Robitaille for his assistance with the hardware side of an electro-mechanical wavelength control system for the laser, as well as his work on a data-acquisition GUI, his significant help in problem solving, and his general assistance with lab work and running experiments, for which I am very grateful. I would like to thank the other members of my group, including Taehyun Yoon, HeeBong Yang, and AJ Malcolm for their work with me on other projects, and, with the addition of Anya Houk and Mai Sakuragi, for their camaraderie, support, and kindness.

I would like to thank Lukasz Komza for the GUI application he wrote to interface with a temperature controller used in the project, as well as Henry Xi for his work on a piece of embedded firmware and a GUI application facilitating computer control of the laser's wavelength. I would like to thank Ruhanshi Barad for her work on a 3D rendering of the optical layout of the laser system.

I would like to thank Prof. Choi and the UQML group for assistance with parts and several electronic control components utilized in this project, as well as Prof. Choi and Hyeran Kong for their advice, explanations, and help regarding the laser system itself. I would also like to thank Roberto Romero for the use of his lab space, supplies, and machining equipment, as well as other members of the IQC such as Steve Weiss for their support in a number of capacities both related and unrelated to this project.

I would like to thank my parents, Brian and Sandy Gross, for their constant love and support, even when facing challenges of their own at the same time. I would like to thank my significant other, Chiara, for her love, patience, and for helping me to take care of myself. I would like to thank all of my friends, for listening, laughing, and for the kindness and love that they show.

Dedication

This thesis is dedicated to my father and mother, Brian and Sandy Gross.

Table of Contents

List of Tables	ix
List of Figures	x
List of Abbreviations	xv
1 Introduction	1
1.1 Rydeberg Excitons in Cu ₂ O	3
1.2 Research Objectives	6
2 ECDL Construction	7
2.1 Contribution Statements	7
2.2 An External Cavity Laser	8
2.2.1 Theory	8
2.2.2 Construction	11
2.2.3 Optical Setup	12
2.2.4 Collimation	13
2.2.5 Grating Alignment	14
2.2.6 Fiber coupling	15
2.3 Fabry–Pérot Cavity	17
2.3.1 Theory	17

2.3.2	Construction	20
2.3.3	Optical Setup	22
2.3.4	Alignment	23
2.4	Characterization	25
2.5	Second Harmonic Generation	26
2.5.1	Theory of Second Harmonic Generation	26
2.5.2	Components and Optical setup	28
2.5.3	Alignment	29
2.5.4	Locking	32
2.6	Characterization	33
2.7	Electronic Control and Laser Stabilization	34
2.7.1	The Pound–Drever–Hall Laser Stabilization Method	34
2.7.2	Signal Routing	36
3	Sample Measurement and Analysis	40
3.1	Contribution Statements	40
3.2	Experimental Setup	41
3.3	Data Analysis	43
3.4	Discussion	50
4	Conclusion	57
4.1	Reflections	58
4.2	Practical lessons	59
4.3	Fulfilment of Objectives	59
4.4	Future Prospects	60
References		61
APPENDICES		67

A Asymmetric Lorentzian Fitting	68
A.1 Background Removal	68
A.2 Fitting Multiple Peaks	69
A.3 Fitting Constraints	70
A.4 Residual Background and Fitting Boundaries	71
A.5 Fitting the Final Peak	72
A.6 Other Fitting Attempts	72

List of Tables

3.1	Constants listed in [1], used in Eq. 1.4 to calculate the portion of the absorption background arising from the Γ_3^- phonon to 1S yellow and green exciton transitions.	52
3.2	Fit values for the parameters of Eq. 1.3, using three different data series. *Values are reproduced from [2] as a basis for comparison to the high resolution absorbance scan and white light absorption spectrum produced here.	55
3.3	Values for E_g and R_y extracted by fitting Eq. 1.2 using the E_n values obtained by fitting the asymmetric Lorentzian. *Values are reproduced from [2] as a basis for comparison to the high resolution absorbance scan and white light absorption spectrum produced here. † In this case, a value for E_n for $n = 3$ is "borrowed" from the E_n fit to the white light data.	55

List of Figures

1.1	A plot of $-R_y/n^2$ from $n = 1$ to $n = 5$. The value chosen for R_y was 92 meV, from [3].	3
2.1	The Littrow ECDL configuration, in which the first order diffraction from a diffraction grating is reflected directly back into the laser diode to provide optical feedback. The grating can be rotated, changing the angle between the incident light and the grating normal, which in turn tunes wavelength of the laser. This also changes the angle of the zeroth order output beam.	9
2.2	The Littman-Metcalf ECDL configuration, in which the first order diffraction from a diffraction grating is reflected off of a mirror, back against the diffraction grating, and into the laser diode to provide feedback. Wavelength in this configuration is controlled by angling the mirror instead of the grating, leading to a fixed output angle for the zeroth order output beam.	10
2.3	An image of the Innolume laser diode used in the ECDL, taken using an optical microscope.	11
2.4	(a) A side view of the collimation package. (b) a view depicting the laser diode package with the TO-56 adapter (used here as a spacer). (c) The back view of the collimation package, where a retaining ring holds the gain stripe package in place. Images captured by Dr. Daniel Kang.	12
2.5	A diagram of the optical elements relating directly to the ECDL and to the fiber couple. Inside the laser cage of the ECDL is a laser diode housed in a collimation package and a diffraction grating.	13

2.6	A closeup of Eq. 2.5 centered around a resonance point ($\lambda_{center} = 1143.074\text{81 nm}$, chosen arbitrarily as one of the resonance points within the working range of the laser diode), evaluated with the parameters $L = 15\text{ cm}$ with mirrors having $r = 99.8\%$. There is an obvious sharp dip in the reflected power around a single wavelength, indicating that theoretically, the incoming field couples almost completely to the cavity at this wavelength. These resonances repeat (infinitely) many times, spaced out by ν_{FSR}	19
2.7	A cross sectional view of a 3D rendering of the FP cavity.	20
2.8	A cutaway showing the FP cavity assembly housed inside a metal flange.	21
2.9	The FP cavity with dimensions of note given labels, and the center of the cavity being defined as $x = 0$	22
2.10	A diagram of the optical setup of the FP cavity component of the system, in isolation from the rest of the system for clarity.	22
2.11	An example of the interference pattern generated by the cavity transmission, imaged by a CCD camera. Note that the interference pattern is spread out on a diagonal, indicating that adjustment of both the horizontal and vertical axis of the alignment mirrors is necessary to better align the cavity.	24
2.12	After further aligning the cavity, the transmission pattern should shrink, and begin to take the form of distinct Hermite-Gaussian modes, like the (a) 00, (b) 10, and (c) 20 modes shown here. Of note is that the modes of the cavity do not have to be exactly these modes to indicate good alignment (e.g. they could include 02 instead of 20), but should include at least the 00 mode.	25
2.13	A diagram of the optical setup of the cavity enhanced SHG component of the system, in isolation from the rest of the system for clarity.	28
2.14	The dimensions of the bowtie cavity. Drawing is not to scale.	29
2.15	The crystal holder assembly. The crystal is heated to the non-critical phase matching temperature using a TEC, whose heat is conducted by a machined copper holder. Other components are used to mate the TEC/Copper arm to a 360° rotational stage, which is then mounted on an xyz-positioning stage, of which only the very top is shown in this figure.	30
2.16	An oscilloscope trace showing the strength of the signal reflected off of the cavity as measured by a photodetector (blue trace) when sweeping a triangle wave across the piezo of mirror M7 (purple trace). An image of the resulting cavity transmittance corresponding to the deepest peaks is inset.	32

2.17	The error signal obtained via the PDH method, simulated for a FP cavity with the parameters $L = 15$ cm and mirrors of $r = 99.8\%$, with a modulation frequency of 9.6 MHz around a resonance point at $\lambda_{center} = 1143.074\,81$ nm. Typically, the error signal would be considered in terms of frequency, but it was kept in the wavelength domain for the sake of comparison to Fig. 2.6.	36
2.18	A block diagram representing the interconnection of the various signal paths and forms of electronic control.	39
3.1	A diagram of the optical setup used to illuminate the Cu ₂ O sample with both the yellow SHG laser light and a white light source.	42
3.2	Voltage signals sampled by ADC from the two imaging PDs, depicting one offset-knob rotation based scan from 1152.85 nm to 1153.07 nm ($\delta_{scan} \approx 0.2$ nm). Each point has an associated wavelength measurement, indicating the fundamental laser's wavelength at that point in time. Variation in the height of the signal is caused by two factors. Varying the wavelength changes the output angle of the laser from the laser cage, which changes the strength of the laser's coupling to the fiber couple (C1, 2.5). The other cause of the variation is a change in the resonant characteristics of the cavity over time. This can be caused by a number of factors including temperature variation and air currents. For some conditions, the cavity parameters change significantly enough that the 2 V _{pp} output of the moku (amplified to 40 V _{pp} by the HV amplifier) is insufficient to reach a resonance point.	44
3.3	A closeup of the 10 s region from 3.2, revealing that the areas of higher voltage signal are actually clusters of very narrow voltage spikes. The main spikes are all spaced approximately 0.1 s apart, corresponding to resonances crossed by the 10 Hz triangle wave. Medium sized peaks and small peaks very close to the noise floor, probably corresponding to other cavity modes. Additionally, a small DC bias, different for both signals, is visible.	45
3.4	A further closeup of a clearly defined single peak, showing the Sampler PD signal closely mirroring the transmission signal in shape, only at a smaller scale. The DC offset has also been removed from the signals, and the maximum of each peak labeled. The Pearson correlation between the two signals is $\rho = 0.9028$.	46

3.5	A closeup of a much noisier pair of peaks. In this case, the sampler signal is just barely above the noise floor, and the actual location of the peak is poorly defined. As a result, normalizing the height of the transmission peak, which in and of itself is somewhat noisy, with the sampler signal is suspect at best. The Pearson correlation between the two signals is only $\rho = 0.5473$	47
3.6	A high resolution laser light transmission scan over the range of 575 nm to 576.5 nm, constructed by normalizing the height of peaks in the transmission PD signal with the sampling PD signal, and plotting the resulting ratio as a function of wavelength. Segments of signals with $\rho < 0.9$ were rejected. The high resolution scan was also normalized with respect to any wavelength dependence of the beam sampler using measurements taken through a window in the sample holder as opposed to transmission through the sample. Also plotted is a white light transmission spectroscopy signal for comparison to the high resolution scan. Both signals have been normalized to have a maximum value of 1 for comparison.	48
3.7	(a) The spectral response of the Princeton spectrometer to SHG light produced with a fundamental wavelength of 1149.574 nm, as measured by the Angstrom wavelength meter. The maximum of the peak occurs at 574.586 nm. (b) The spectral response of the Thorlabs CSS compact spectrometer to the same light as the Princeton spectrometer. The resolution of this small device is noticeably worse, as is to be expected of its small size. The maximum of the peak occurs between 574.505 nm and 574.666 nm.	49
3.8	The signal from Fig. 3.6 after being filtered with a 1000 sample rolling average filter, and offset by 0.2 nm to account for the systemic error in the Angstrom wavelength meter.	50
3.9	The high resolution scan and white light transmission spectra, transformed to be in terms of Energy and Absorbance. Also shown is the calculated phonon background signal.	51
3.10	The ECDL based high resolution spectral scan and white light absorbance spectroscopy signals overlaid on top of another white light absorbance spectrum, reproduced using data from [2]. The white light and scan data have been scaled to the same scale as the reproduced data, for the sake of a direct comparison of the values obtained by fitting Eq. 1.3 to each peak.	53
3.11	The fit line obtained when fitting a sum of asymmetric Lorentzians to the high resolution spectral scan. Only two peaks, corresponding to the $n = 4$ and $n = 5$ resonances were fit.	54

3.12 $E_g - E_n$ vs n , for each of the three data series, plotted on a log-log scale to make the exponential scaling appear linear. A guideline scaling with exactly n^{-2} is added for visual comparison, showing that the scaling of the experimental E_n s deviates from the expected scaling rate, but not significantly. Notably, the two data points from the high resolution scan are on trend with the rest of the data.	56
A.1 An example of an attempt to fit the asymmetric Lorentzian to the resonance peaks one at a time. Generally, the quality of the fitting is bad, specifically in the valleys between peaks. Reproduced absorption spectra data of the green exciton at 4K using data from [2]	69
A.2 The same 4 K green exciton spectra, this time with all peaks being fit simultaneously using a superposition of asymmetric Lorentzian functions. Although the quality of the fit looks much better visually, the values of the extracted physical parameters are nonsensical. Reproduced using data from [2]	70
A.3 An example of the Green exciton series at 70 K. The $n = 3$ and $n = 4$ peaks are beginning to overlap significantly due to thermal broadening effects, which makes fitting each peak individually difficult. Reproduced using data from [2].	73

List of Abbreviations

ADC analog to digital converter xii, 41, 44

AFG arbitrary function generator 32, 36, 37

AR anti-reflection 8, 28, 41

CDF cumulative distribution function 73

CPM critical phase matching 27

DAC digital to analog converter 37, 42

ECDL external cavity diode laser x, xiii, 2, 6, 8–10, 12, 43, 53, 57, 59

EOM electro-optic modulator 23, 36

FG function generator 37

FP Fabry–Pérot xi, xii, 6, 7, 15–18, 20–26, 31, 32, 34–37, 41, 42, 57, 59, 60

FSR free spectral range 17, 18, 26, 33, 59

FWHM full-width half-maximum 4, 18, 26

LBO Lithium triborate LiB₃O₅ 28

NCPM non-critical phase matching 27, 28

PBS polarizing beam splitter 23, 24

PD photodetector xii, xiii, 29, 41, 43–46, 48

PDH Pound–Drever–Hall xii, 7, 18, 32–34, 36, 37, 57

QWP quarter-wave plate 23

SFG sum frequency generation 60

SHG second harmonic generation xii, xiii, 2, 6, 7, 15, 16, 26, 28, 32, 33, 37, 40–43, 46, 47, 49, 50, 57, 59, 60

SNR signal to noise ratio 45, 46

Chapter 1

Introduction

The search for a suitable quantum information processing platform is still an open one full of many promising candidates, each of which has their own advantages and disadvantages. Currently, the most successful technologies (going by record numbers of qubits) are trapped ion and superconducting qubit based quantum computers, but both schemes are beginning to face issues with scaling beyond ≈ 50 qubits [4]. This opens the door for the development of other technologies, which may be able to overcome such limitations.

One such competing technology is based on neutral atoms, which implement qubits via arrays of interacting neutral atoms. Since the atoms are electrically neutral, interaction is facilitated by putting atoms into a so-called Rydberg state[5], in which an electron becomes highly excited but is still bound to the atom. Such Rydberg atoms have a huge dipole moment allowing for long range interactions. This includes an effect known as the Rydberg blockade, in which the excitation of one atom shifts the energy levels of Rydberg states for nearby atoms, effectively suppressing the further transitions to Rydberg states within a neighborhood [3, 5]. The Rydberg blockade can then, in turn, be used to implement two-qubit gates [5].

Interestingly, atomic systems are not the only environments where Rydberg states have been observed. In semiconductors, electron hole pairs can become bound together in a hydrogen-like state called an exciton [6, 7, 8]. These excitons can also exhibit the highly excited Rydberg states seen in atoms, leading to the formation of Rydberg excitons, and allowing for the possibility of implementing a Rydberg interaction based quantum information processing system in solid state semiconductors [9, 10, 11].

Among the field of candidates for a viable solid state quantum simulator, cuprous oxide Cu_2O shows promise thanks a relatively high Rydberg energy ($R_y \approx 90 \text{ meV}$) [12] and a

series of well defined exciton resonance peaks with a number of desirable properties. The yellow P-series in particular shows stability in peaks corresponding to $n = 8$ at or even above liquid nitrogen temperatures [2], and at low temperatures (110 mK) peaks as high as $n = 28$ have been imaged using high resolution spectroscopy [13].

Higher n peaks can have more desirable properties, such as huge radii and dramatically increased lifetimes (on the order of nanoseconds)[3]. However, as n increases, the width of each exciton resonance peak decreases with n^{-3} [14, 2] , quickly reaching the point where imaging the peaks using traditional transmission spectroscopy with a broad spectrum light source and diffraction spectrometer becomes impossible (e.g. $n = 24$ exhibits a linewidth of 3 μeV [3]). An alternative is to scan the wavelength of a very narrow line-width laser and measure the intensity of the transmission through the sample at each wavelength in order to create a high resolution spectral scan. Unfortunately, the Yellow P-excitons in Cu₂O inhabit the neighborhood of ≈ 571 nm (depending on the temperature of the sample), a range for which commercial tunable lasers, or even commercial laser diode, options are limited. One approach to create a tunable laser light source at the desired wavelength is to use a commercial laser diode in an [external cavity diode laser \(ECDL\)](#) configuration (allowing for tunability), and then through a process known as [second harmonic generation \(SHG\)](#), to double the frequency of the light, which in the case of the system described in this thesis, allows for the conversion of infrared light to visible yellow light in the wavelength range necessary to perform such a scan.

As previously alluded to, this thesis describes the design and construction of one such laser system, and its usage in a preliminary experiment to perform a high resolution scan of a portion of the yellow P-exciton series in Cu₂O at a cryogenic temperature of 100 K.

Beyond facilitating high resolution spectral scans (which themselves can be expounded upon by examining the effects of, for example, an external electric field [12], or further study of the so-called quantum defect [15]), a narrow linewidth tunable laser allows for excitation of individual energy levels, which when combined with a second laser could allow for pump-probe experiments to further explore the Rydberg blockade effect in excitons [3, 16], and effects like electromagnetically induced transparency [17]. The ability to probe individual states which interact strongly with neighboring states, coupled with the ability to control those interactions through effects like the Rydberg blockade, all works towards the goal of creating scalable quantum logic gates with which to implement a quantum information processing system [9, 10, 11].

1.1 Rydberg Excitons in Cu₂O

Cu₂O is a direct bandgap semiconductor [18, 3], which supports yellow exciton transitions between the Γ_6^+ conduction band and Γ_7^+ valence band, green transitions between the Γ_6^+ conduction and Γ_8^+ valence bands, blue transitions between the Γ_6^- conduction and Γ_7^+ valence bands, and violet transitions between the Γ_6^- conduction and Γ_8^+ valence bands. In the case of the yellow and green excitons, the S-exciton series is dipole forbidden, and as a result, cannot be accessed via spectroscopy. The P-exciton series for both, on the other hand, is dipole allowed, and can be seen riding a top a thermal phonon background via absorption spectroscopy techniques [1, 3].

Since the exciton series are hydrogen-like, they follow the well known Rydberg equation, where the distance from the band gap energy E_g for each n energy level is:

$$E_n = E_g - \frac{R_y}{n^2} \quad (1.1)$$

with the different colored series having different values for R_y . For the yellow excitons, R_y is typically reported to be between 87 - 92 meV [1, 3, 15]. Plotting $-R_y/n^2$ for $n = 1-5$ (Fig. 1.1) reveals a series of energy levels which indeed closely resembles the classic hydrogen energy level diagram.

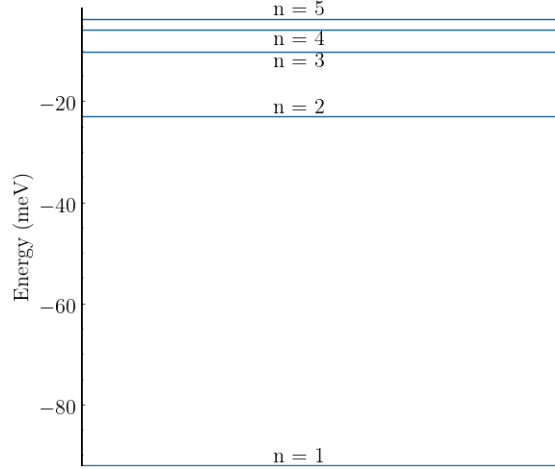


Figure 1.1: A plot of $-R_y/n^2$ from $n = 1$ to $n = 5$. The value chosen for R_y was 92 meV, from [3].

Frequently Eq. 1.1 is modified by an additional term δ , called the quantum defect, to account for a observed deviation from the hydrogen-like Rydberg formula in excitons due to splitting between states of different angular momentum [3, 15, 19]. This gives:

$$E_n = E_g - \frac{R_y}{(n - \delta)^2} \quad (1.2)$$

However, the effect of the quantum defect, including whether or not is constant or dependent on n , l , or some other factor, and what the value or values that it takes are, are still actively being studied [15].

The absorption lines of the P-excitons are described by a series of asymmetric Lorentzians as shown by Toyozawa, with the equation for a single peak given by [14]:

$$\alpha_n(E) = C_n \frac{\frac{\Gamma_n}{2} + 2Q_n(E - E_n)}{\left(\frac{\Gamma_n}{2}\right)^2 + (E - E_n)^2} \quad (1.3)$$

where C_n is a term describing the oscillator strength, Γ_n is the **full-width half-maximum (FWHM)** line-width of the resonance peak at the energy E_n , and Q_n captures the asymmetry. The parameters of Eq. 1.3 each follow a set of well known scaling laws as a function of n , the principle quantum number corresponding to each peak [2]. Together these terms characterize a resonance peak, and can be used to perform deeper analysis such as calculating E_n and R_y and estimating the exciton lifetime [3].

The exciton resonance peaks ride atop a broad background spectrum, which in the energies the yellow P-excitons occupy is comprised of contributions from the phonon-assisted transitions from Γ_3^- to the 1S Yellow and Green excitons [1], as well as absorbance from the Urbach tail and P-exciton continuum.

The absorption spectrum for the phonon assisted absorption is derived in [1] for the yellow P-excitons as:

$$\alpha_{n,y}^\lambda(\omega) = \frac{e^2}{\pi^2 \hbar \rho \epsilon_0 n_R c a_b^3} \frac{M_y}{m_0} \frac{q_n^\lambda}{\omega \omega_\lambda} \frac{|p_{78}|^2}{m_0} |D_{\lambda;68}(q_n^\lambda)|^2 \times \left| \sum_{n'} \frac{\mathcal{S}_{n,n'}^{(y,b)}(q_n^\lambda)}{n'^{3/2} (E_{n'S}^{(b)} - \hbar \omega)} \right|^2 \Theta(q_n^\lambda) \quad (1.4)$$

where the term q_n^λ , with λ as an index denoting a specific phonon such as Γ_3^- or Γ_4^- , is defined as:

$$q_n^\lambda(\omega) = \sqrt{\frac{2M_y}{\hbar^2}} \sqrt{\hbar \omega - \hbar \omega_\lambda - E_{nS}^{(y)}} \quad (1.5)$$

and e is the charge of an electron, ρ is the density, n_R is the refractive index at the exciton energy, a_b is the blue exciton's Bohr radius, M_y is the mass of the yellow exciton, m_0 is the mass of a free electron, $\hbar\omega_\lambda$ is the energy of the phonon indexed by λ , p_{78} is the term for dipole transitions between Bloch states, $D_{\lambda;68}$ is the deformation potential (with $D_{\lambda;68}(Q) \approx D_{\lambda;68}^{(0)} \left(1 + D_{\lambda;68}^{(2)} Q^2\right)$), $E_{nS}^{(y)}$ ($E_{nS}^{(b)}$) is the nS yellow (blue) exciton energy, and $S_{n,n'}^{(y,b)}$ is the yellow and blue exciton overlap factor given by:

$$S_{1,1}^{(y,b)}(Q) = \frac{2^7 \beta^{3/2} (1 + \beta)}{(4(1 + \beta)^2 + \alpha_y^2 \beta^2 Q^2)^2} \quad (1.6)$$

with $\beta = a_b/a_y$ [1].

Also formulated by [1] is the P-exciton continuum:

$$\alpha_{P\text{cont}}(\omega) = C_{yP} \frac{(\hbar\omega - \tilde{E}_g)^{3/2}}{\hbar\omega} \frac{\gamma e^\gamma}{\sinh \gamma} \left(1 + \frac{\gamma^2}{\pi^2}\right) \quad (1.7)$$

with $C_{yP} = 9.82 \times 10^{-2} \sqrt{\text{eV}} \mu\text{m}^{-1}$ as a material constant and γ defined as:

$$\gamma = \sqrt{\frac{\pi^2 \text{Ry}_y}{\hbar\omega - \tilde{E}_g}} \quad (1.8)$$

consisting of the yellow Rydberg energy $\text{Ry}_y = 87 \text{ meV}$ and the renormalized band gap energy $\tilde{E}_g = E_g + \Delta_c$ (with Δ_c approximated as $-\text{Ry}_y/n_{\max}^2$).

Finally, the Urbach tail's [20] contribution to the background absorption is the formulated by [1] as:

$$\alpha_{\text{Urbach}}(\omega) = C_U \exp\left(\frac{\hbar\omega - \tilde{E}_g}{E_U}\right) \theta(\tilde{E}_g - \hbar\omega) \quad (1.9)$$

which includes the constants $C_U = 7.34 \times 10^{-3} \mu\text{m}^{-1}$ and $E_U = 9.8 \text{ meV}$.

1.2 Research Objectives

The the research project outlined in this thesis consists of several steps. The first is to construct a narrow linewidth tunable laser, in this case an ECDL with an Fabry-Pérot (FP) cavity to act as a stable wavelength reference, and a SHG module for converting the infrared fundamental light of the laser into the yellow light required by the experiment, all of which are described in detail in Chapter 2. Such a system needs to be characterized, after which the intent is to use the laser to conduct an experiment. For the scope of this thesis, the goal is to use the laser in order to perform a high resolution spectral scan of the yellow P-exciton series in Cu₂O, with the aim of specifically targeting resonances corresponding to $n > 11$ at 4 K, as in a previous study these peaks were not resolvable with traditional spectrographic techniques [2]. The results of the experiment then need to be analyzed in order to evaluate the efficacy of the high resolution scan, before the laser can be used in further experiments outside the scope of this thesis.

Chapter 2

External Cavity Laser Diode System Construction

This chapter is an overview of the design and construction of a narrow linewidth wavelength tunable laser system, capable of producing output light suitable for a high resolution spectral scan of the yellow P-exciton series in Cu₂O. The laser system itself consists of several components, including an infrared laser light source utilizing an external cavity configuration, a stable wavelength reference in the form of an FP cavity, a bowtie-cavity enhanced SHG module to double the fundamental infrared wavelength of the laser to yellow light, and the electronic feedback and control systems for laser and cavity stabilization using the Pound–Drever–Hall (PDH) method.

2.1 Contribution Statements

The design work of the laser system described in this chapter was performed by Prof. Kyung Soo Choi, Prof. Na Young Kim, Dr. Daniel Kang, Younseok Lee and Hyeran Kong based on the ECDL lasers described in [21], with the design of the FP cavity based on [22], and the non-linear crystal holder designed by Prof. Na Young Kim, Daniel Kang, and the author. The construction of the laser system was performed by Dr. Daniel Kang, Hyeran Kong, the author, Marcel Robitaille, and Prof. Na Young Kim, with components such as a laser control box and laser cage provided by Prof. Choi’s UQML group and prepared by Prof. Na Young Kim, Dr. Younseok Lee and Hyeran Kong.

2.2 An External Cavity Laser

The **ECDL** is comprised of a number of optical systems, one of which is the source of the light itself. While the entire system is frequently referred to as the **ECDL**, the real **ECDL** is only the subsystem consisting of a semiconductor laser gain material and diffraction grating used to form an optical resonance cavity external to the semiconductor gain material, hence the name **external cavity diode laser**. The primary advantage of an **ECDL** over other laser systems is the ability to tune the wavelength of the laser over a broad range via the diffraction grating, while still maintaining a fairly narrow line-width.

2.2.1 Theory

Spontaneous emission is a phenomenon in which an excited electron randomly decays to a lower energy state, releasing a photon in the process. This is seen for example, in LEDs, where a voltage applied across a PN-junction creates excited electron-hole pairs whose recombination leads to the emission of light. Laser diode operation is predicated on stimulated emission, in which an incident photon interacts with an electron in an excited state, causing the electron to decay and release a photon in the same mode (i.e. same wavelength, polarization, and direction of travel) as the stimulating photon. This effectively creates an amplification effect. Stimulation is achieved in laser diodes through the use of an optical cavity, in which spontaneously emitted photons are reflected back and forth between two reflective surfaces, during which they interact with the semiconductor material. This leads to a large amount of stimulated emission in a runaway effect, and creates a coherent laser beam from the photons that leak from the optical cavity [23].

In conventional laser diodes, the optical cavity is typically formed at the boundaries of the gain material by coating the front and back facets of the semiconductor with a highly reflective material, creating an optical cavity entirely within the diode itself. In an **ECDL**, however, (at least) one end of the diode is **anti-reflection (AR)** coated, with a mirror or diffraction grating used to complete the optical resonance cavity. In this case, part of the cavity is external to the gain material itself, hence the name of the configuration. The formation of an external cavity has several advantages including decreasing laser linewidth [24], but critically for the application of broadband scanning of a laser, it allows for selectivity of the optical feedback which stimulates lasing in the gain material. Specifically, a diffraction grating can be used to select a specific wavelength of light for feedback, and due to the coherent nature of stimulated emission, this can be used to tune the wavelength of the emitted light over a far broader range than can be achieved by techniques such as varying the injection current or temperature of the gain material [24].

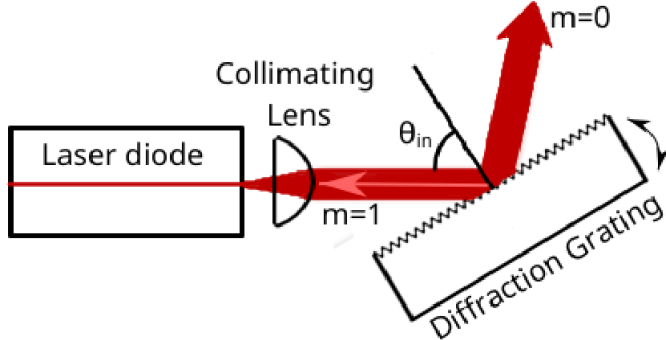


Figure 2.1: The Littrow ECDL configuration, in which the first order diffraction from a diffraction grating is reflected directly back into the laser diode to provide optical feedback. The grating can be rotated, changing the angle between the incident light and the grating normal, which in turn tunes wavelength of the laser. This also changes the angle of the zeroth order output beam.

ECDLs are typically constructed in one of two configurations: the Littrow or Littman-Metcalf configurations. In the Littrow configuration [25], an example of which is shown in Fig. 2.1, the first order diffraction from a diffraction grating is used for optical feedback to generate stimulated emission, with the zeroth order diffraction acting as output [26, 24]. The Littrow configuration is achieved by choosing the blaze angle of the grating such that the diffracted light (usually first order) is reflected back towards the light incident on the grating at the same angle. In this case, the diffraction efficiency for that order of light is maximized, thereby maximizing optical feedback to the laser diode [27]. The grating equation is:

$$m\lambda_L = d (\sin \theta_{in} + \sin \theta_{out}) \quad (2.1)$$

where d is the groove spacing of the grating, m is the diffraction order (0 for the main beam which reflects off of the grating, 1 for the first order diffraction used as optical feedback, etc.), θ_{in} is the angle from the incident beam to the grating normal, θ_{out} is the angle of the m^{th} order refracted beam, and λ_L is the wavelength of the beam [27, 28]. For the Littrow configuration, $\theta_{in} = \theta_{out}$, yielding:

$$m\lambda_L = 2d (\sin \theta_{in}) \quad (2.2)$$

This means that the output wavelength can be adjusted by adjusting the angle between

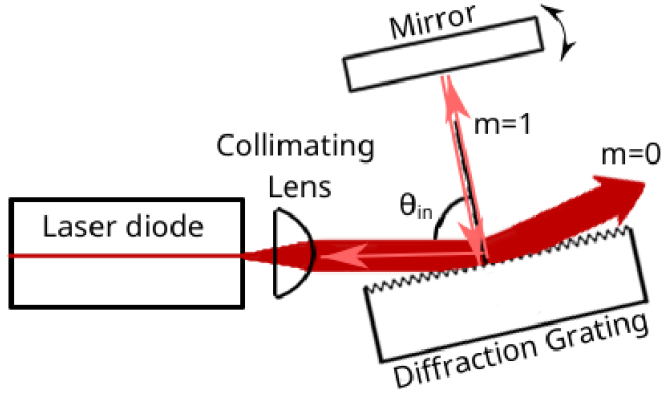


Figure 2.2: The Littman-Metcalf ECDL configuration, in which the first order diffraction from a diffraction grating is reflected off of a mirror, back against the diffraction grating, and into the laser diode to provide feedback. Wavelength in this configuration is controlled by angling the mirror instead of the grating, leading to a fixed output angle for the zeroth order output beam.

the incident beam and normal of the grating, usually achieved by rotating the grating. This has the notable effect of changing the angle of the zeroth order output beam as well [28, 26].

In the Littman-Metcalf configuration, originally introduced in [29] and [30] for application with pulsed dye lasers and an example of which is shown in Fig. 2.2, the incident beam is aimed at a grazing angle relative to the grating. The first order diffraction then reflects off of a mirror, back into the diffraction grating, and into the laser to provide the feedback. In this configuration, angle of the mirror, and not the grating, is rotated to vary the wavelength, meaning that the angle of the output beam is fixed. However, this configuration has the drawback that it is more complex than the Littrow configuration, and suffers from lower power output [26, 28].

In the case of the **ECDL** described in this thesis, the gain material is a thin semiconductor straight stripe gain strip, with a highly reflective back facet and an AR coated, Brewster cut front facet. The shape of the front facet is rectangular, as shown in Fig. 2.3. This means that the resulting beam is slot/elliptically shaped, with a high degree of eccentricity. In addition, the angle of divergence along the horizontal and vertical axis of the emitting face differ, leading to an astigmatism, where the two axes of the emitted laser beam focus at two different lengths [31].

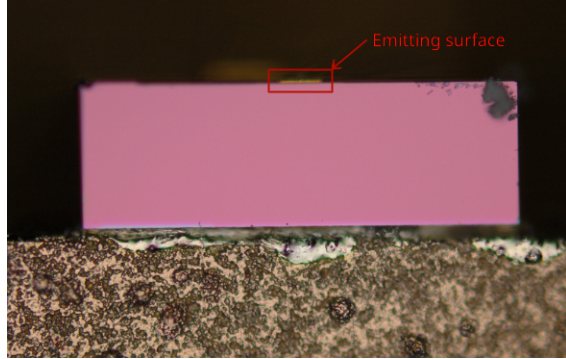


Figure 2.3: An image of the Innolume laser diode used in the ECDL, taken using an optical microscope.

2.2.2 Construction

The laser diode used is an Innolume GC-1160-90-TO-200-A stripe gain chip with a typical wavelength of maximum power of 1160 nm. This is housed in a Thorlabs LT230P laser collimation package, with a C330TMD-C lens used for collimation. The collimation package is designed for a typical TO-9 can laser diode, the dimensions of which the laser diode does not conform to. In order to retrofit the nonstandard package to work with a standard collimation package, the provided TO-56 can diode adapter is used as a spacer to keep our laser diode (which has a long gain strip) at a sufficient distance from the collimation lens such that focusing is possible. The rim of the base flange of the laser diode chip package is also coated in 3 layers of clear acrylic nail polish to extend the diameter slightly so that it sits centered in the collimation package.

The diffraction grating is a Richardson 33025FL01-220H (1200 g/mm, blaze wavelength of 700 nm), which is mounted in a Littrow configuration on an two axis adjustable holder, with a piezo actuator allowing for modulation of the horizontal axis.

Both the collimation package and diffraction grating are mounted in a custom laser cage developed by the UQML group [21] with an integrated thermoelectric cooler. The leads on the back of the gain stripe package plug into a static discharge protection circuit, with wires conducting the current to this circuit exiting out of the back of the laser cage.

Figure 2.4 depicts the collimation tube, starting with the assembled package with the static protection circuit attached in a). To assemble the collimation tube, start by applying 3-4 coatings of clear acrylic to the circumference of the base of the laser diode package. Test the fit in the collimation tube to ensure that it is snug. If the fit is too loose, add



Figure 2.4: (a) A side view of the collimation package. (b) a view depicting the laser diode package with the TO-56 adapter (used here as a spacer). (c) The back view of the collimation package, where a retaining ring holds the gain stripe package in place. Images captured by Dr. Daniel Kang.

more acrylic. If it is too tight, apply some acetone with a cotton swab to remove some of the acrylic. Once the fit is right, place the spacer on the gain stripe package as shown in Fig. 2.4 b), and then insert the it into the collimation package. Secure it with the retaining ring as shown in Fig. 2.4 c). Insert the collimation lens on the other end of the package, and plug the laser diode into the socket on the anti-static board, being careful to respect the orientation of the pins on the gain stripe and socket. The pins are asymmetrical and should be able to be plugged in only one way, but are flexible enough that it might be possible to insert the it in the incorrect orientation.

2.2.3 Optical Setup

Figure 2.5 shows the optical elements associated with the ECDL, from the generation of light in the laser cage up until the second fiber couple (labeled C2). The first element the laser beam encounters upon exiting the cage is a Thorlabs PS883-C mounted prism pair with $4\times$ magnification, which is mounted in reverse to shrink the laser beam along the horizontal axis by $4\times$, reducing the eccentricity of the beam significantly. Having been shrunk to a suitable size, the beam passes through a Thorlabs IO-4-1150-VLP optical isolator, which prevents back reflections into the gain material which could damage or ultimately destroy it. From here, the beam passes through a plano-convex mirror, L1, which is used to focus it ahead of the lens incorporated into the fiber couple itself, and was found in practice to increase the efficiency of the power coupling through the fiber optic cable. The laser is then directed to the fiber couple by two steering mirrors, M1 and M2, allowing for four degrees of freedom which are used to precisely align the laser beam with the fiber optic cable input and maximize the power coupled to the fiber. The fiber

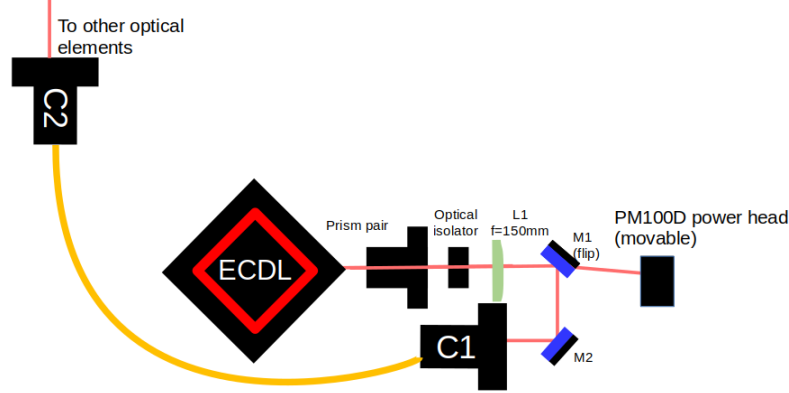


Figure 2.5: A diagram of the optical elements relating directly to the ECDL and to the fiber couple. Inside the laser cage of the ECDL is a laser diode housed in a collimation package and a diffraction grating.

couple, C1, consists of a two axis adjustable mount and two components: a focusing lens (Thorlabs C330TMD-C) and an FC fiber termination into which an Oz Optics SMJ-3A3A-1060-6/125-3-2 single mode patchcord fiber optic cable is inserted.

2.2.4 Collimation

Collimation of the light emitted from the laser diode and the alignment of the diffraction grating go somewhat hand-in-hand. Without either, the laser will not lase, even at very high currents (500 mA) due to a lack of optical feedback. If the laser diode is not lasing, it is hard to fine tune the collimation precisely due to low beam power making it difficult to visualize the beam profile. Therefore, it may be necessary to first roughly collimate the beam to a reasonably long focal length or small divergence, then align the grating, then precisely collimate the beam and finally fine tune the grating alignment.

Collimation of the beam is performed without any any additional beam shaping elements besides the collimation lens housed in the collimation package. Thus, the prism pair, optical isolator, and L1 are removed. Collimation is also best performed over a long distance (2 or more meters) in order to obtain a precise alignment. To do so, a mirror was used to direct the beam of the laser down the long axis of the optical table towards a wall where an IR viewing card was taped to visualize the beam profile. The mirror was

mounted on a flip mount, so that when not looking at the beam shape it could be diverted from the IR card to prevent overexposure. It is also useful to have a second IR card on hand to visualize the profile of the beam in free spaces as it is propagating.

Collimation is performed with the collimation package mounted in the laser cage by placing the end of a small hex key in the notch in the metal body of the collimation lens inside the package and using it to rotate the lens, thereby adjusting its position and focus. The goal is to ensure that the beam is not visibly focusing (coming to a single point along one or both axis and then diverging again) at any point along the visible path, or diverging significantly at the end. In practice, the beam may have an astigmatism, meaning that both the horizontal and vertical axis do not focus at the same point, which can make collimation difficult. In addition, the beam will diverge regardless of collimation quality over distances on the scale of the Rayleigh length.

One method to collimate the beam is to adjust the collimation lens until the beam is focusing along at least one axis near the wall used to terminate the beam. Then, adjust the lens very slightly until the focal point of the beam vanishes to a point slightly behind the plane of the wall. This transition is very sensitive, the angle of rotation of the lens needed to achieve this is typically less than 5° .

2.2.5 Grating Alignment

The proper alignment of the diffraction grating is necessary in order to aim the first order diffraction of the laser light back into the the gain material, providing the necessary optical feedback for lasing to occur, and allowing for wavelength selectivity. The vertical alignment is the most crucial, as the horizontal alignment of the grating is frequently slightly misaligned intentionally as this is how the wavelength is changed.

When starting a grating alignment from scratch, e.g. when installing a new laser diode, both the horizontal and vertical axis might be misaligned. To check, first turn the current to the laser diode all the way down to 0 mA, then start to slowly increase it (to a maximum of 500 mA). At some point, the beam should be faintly visible when viewed using an IR card. If the beam suddenly jumps dramatically in brightness at any point, the gain strip is getting enough optical feedback to begin lasing, and the grating is at least partially aligned.

If lasing does not occur at any point, then the grating needs to be completely re-aligned. Start by adjusting the vertical alignment upward so that the first order diffraction beam is angled to hit the laser cage at a height above the collimation package. It may be useful to use a pair of forceps and a small strip of IR card to view the beam in this confined space.

Once the beam is angled up sufficiently, is possible to view the first order diffraction with an IR card (or IR card strip) without blocking the fundamental beam on its path to the diffraction grating from the diode. Next, adjust the horizontal alignment of the grating until the first order diffraction is roughly aligned with the center of the collimation lens on the horizontal axis. It should be directly above the beam coming from the laser diode, before reflection off of the grating. Then, adjust the vertical axis of the beam back down, until the original and reflected beams are roughly overlapping. At this point, visible lasing should occur at a high enough current, and the alignment can be further fine tuned.

To fine tune the grating adjustment, first start with the vertical axis. Turn the laser diode current up until lasing is visible. Then, lower the current until just below the threshold at which lasing occurs. The light on the IR card should appear dim, or flash as lasing occurs intermittently. Adjust the vertical alignment until lasing occurs at the lowered current. Then, lower the current once again until just below the threshold for lasing, and again adjust the vertical alignment to re-initiate lasing. Repeat this process until a current is reached at which lasing will no longer occur regardless of vertical axis adjustment.

In many cases, only the vertical alignment of the diffraction grating needs to be fine tuned, since, as stated previously, the horizontal alignment is intentionally slightly misaligned to adjust the laser wavelength. However, in order to find the maximum power of the laser, the horizontal axis can be aligned in the same manner as the vertical. After adjusting the horizontal alignment a significant amount (even if just to change the wavelength of the laser), it can be useful to re-adjust the vertical alignment as it may have changed slightly. Also, if the laser wavelength is unstable, a slight adjustment of the vertical or horizontal grating alignment can help with stability, although it may lower the laser's output power slightly.

2.2.6 Fiber coupling

When adjusting the wavelength of the laser, the angle of the beam relative to the body of the laser cage changes due to nature of the Littrow configuration used. This change in angle presents a problem with regards to the rest of the optical setup, as the two cavities ([FP](#) and [SHG](#)) used require precise alignment to operate, and are incredibly sensitive to any such changes. In order to counteract this the laser light is routed into a fiber optic cable, the output of which is in a fixed position. Two steering mirrors (M1 and M2) are used to counteract changes to the beam angle due to changing wavelength and direct the light into the input side of the cable via a fiber couple. The coupling to the fiber itself can

be very sensitive and required careful alignment, but this alignment is simpler than having to repeatedly re-align both cavities.

Start off by measuring the power of the laser prior to coupling. This can be done by flipping down M1 and placing the power head of the Thorlabs PM100D behind it. This allows for the estimation of an acceptable amount of power coupled through the fiber optic cable, the efficiency of which should be somewhere around 50%. Flip M1 back up and place the power head at a location after the fiber couple to measure the power transmitted through the fiber optical cable. If the power measured by the meter is less than $1 \mu\text{W}$, adjust the knobs of M1 and M2, watching for any fluctuations in power.

If no fluctuations in power are present, the laser is not coupled to the fiber at all. This can be remedied by roughly aligning the laser using the Oz Optics fiber checker. First, remove the fiber optic cable from C1. It is important to remove it from C1 and not C2, as this keeps C2 fixed. Even slight changes to the position of C2 can require careful realignment of the SHG and FP cavities. Next, attach the Oz Optics fiber checker to C1 using a different fiber patch cable. Position the IR card right before the entrance to C1. Adjust M1 to align the brightest part of the laser light (the red glowing spot on the IR card) with the spot from the Oz Optics Laser source, which should glow yellow-green. Position the IR card right after the optical isolator and adjust M2 to align the ECDL and fiber checker spots at this point was well. Return the IR card to the fiber couple, and repeat the adjustment of M1. Return the IR card to the optical isolator, and repeat the adjustment of M2. Iterate until no deviation in spot position is observed when moving from the fiber couple to the optical isolator or vise-versa. Remove the Oz Optics light source and re-attach the original fiber optic cable. At this point, the laser should be well aligned enough that some transmitted power is measurable.

Once the laser is partially coupled to the fiber optic cable, M1 and M2 can be used to fine tune the alignment and maximize the transmitted power. Start by adjusting both knobs of M1 to maximize the observed power. Then, adjust both knobs of M2 to maximize observed power. Now, adjust one axis of both mirrors simultaneously. For example, return to M1 and starting with the top knob, slightly adjust in one direction. Then adjust the top knob of M2 to re-maximize the power. If the new maximum power is less than before, return to M1 and move top knob in opposite direction, then adjust top knob of M2 to maximize power. Continue to move M1 in the direction of increasing maximum power, using M2 to maximize power, until the max power begins to lower when moving M1 further. Follow the same procedure with the bottom knobs of M1 and M2. Return to the top knobs of both mirrors and follow the same procedure again. Alternate adjusting top and bottom knobs of both mirrors until the max power does not change or go down. The maximum

measured power should be on the scale of 45-50%¹ of the power measured prior to the fiber couple. If a local maximum is found that is significantly less than this value, try adjusting top/bottom knob of M1 in large amounts in either direction until power goes down, then starts to go back up. This is a new local maximum that can be optimized, starting from the beginning of the partially coupled step. If this does not work, it may be best to start again from the basis of being completely uncoupled and repeating the steps using the Oz Optics fiber checker.

2.3 Fabry–Pérot Cavity

A [Fabry–Pérot \(FP\)](#) interferometer, also known as an [FP](#) cavity, is an optical resonance chamber comprised of two mirrors facing each other that resonates only with light which has a wavelength that is an integer multiple of twice the distance between the two mirrors. As such, it can be used to construct an extremely sensitive wavelength reference, which can in turn be used through feedback techniques to stabilize and narrow the line-width of a laser source.

2.3.1 Theory

[FP](#) cavities have the property that they only transmit light at wavelengths which are integer multiples of twice the cavity length, because only under this condition does light which leaked into the cavity after one round trip perfectly match the phase of incoming light. This leads to perfect constructive interference, effectively coupling the electromagnetic field of the laser to the cavity in spite of the (typically) small value of the transmittance coefficient used in the mirrors comprising the cavity. The spacing between two adjacent frequencies of light at which the [FP](#) cavity resonant, called the [free spectral range \(FSR\)](#), is given by [32, 33]:

$$\Delta\nu_{FSR} = \frac{c}{2L} \quad (2.3)$$

¹The fiber coupling efficiency of $\approx 50\%$ mentioned above is still somewhat low, but was the best that could be attained after adapting the nonstandard laser diode package to fit in the Thorlabs collimation tube, many careful collimation attempts, failed attempts to use cylindrical lenses to correct the astigmatism introduced by the shape of the front facet of the gain chip, and attempts to use plano-convex lenses to further condition the beam prior to the fiber couple. The remaining lack of efficiency is attributed to any remaining imperfections of the seating of the gain stripe package in the collimation tube, and the astigmatism of the beam.

where c is the speed of light and L is the spacing between the two mirrors of the cavity.

By observing the intensity of the light reflected off of the cavity and varying the wavelength of said light, it is possible to observe dips in the intensity of the reflected light, which mark resonant wavelengths at which the light is coupling to the cavity. In this way, the cavity acts as a reference for a very specific frequencies of light (spaced out by the **FSR**), which the laser source can in principle be locked to via electronic feedback. The most common method for achieving this laser stabilization is the **PDH** method.

Given an electric field with intensity E_0 and frequency ω incident upon the cavity:

$$E_{inc} = E_0 e^{i\omega t} \quad (2.4)$$

we consider the ratio of the reflected electric field E_{ref} to the incident field when the cavity has symmetric mirrors with reflection coefficient r [32]:

$$H(\omega) = \frac{E_{ref}}{E_{inc}} = \frac{r \left(\exp\left(i \frac{\omega}{\Delta\nu_{FSR}}\right) - 1 \right)}{1 - r^2 \exp\left(\frac{\omega}{\Delta\nu_{FSR}}\right)} \quad (2.5)$$

Choosing values for L and r which match the design parameters for the **FP** cavity used in this experiment, we can see in Fig 2.6 that a resonance occurs at around 1143.07481 nm.

These resonance dips have a bandwidth defined by their **FWHM**, which for a cavity with symmetrical mirrors is theoretically predicted by [33]:

$$\delta_\nu = -\frac{c}{\pi L} \ln(r) \quad (2.6)$$

This can further be used to define two characterizing quantities, the cavity finesse F and quality factor Q [33]:

$$F = \frac{\Delta\nu_{FSR}}{\delta_\nu} = \frac{\pi}{2 \ln(r)} \quad (2.7)$$

$$Q(\nu) = \frac{\nu}{\delta_\nu} \quad (2.8)$$

For the cavity parameters described above, the width of the resonance lines is $\delta_{nu} = 1.273$ MHz, the finesse of the cavity is $F = 784.6$, and the quality factor at 1143.07481 nm is $Q = 2.059 \times 10^8$.

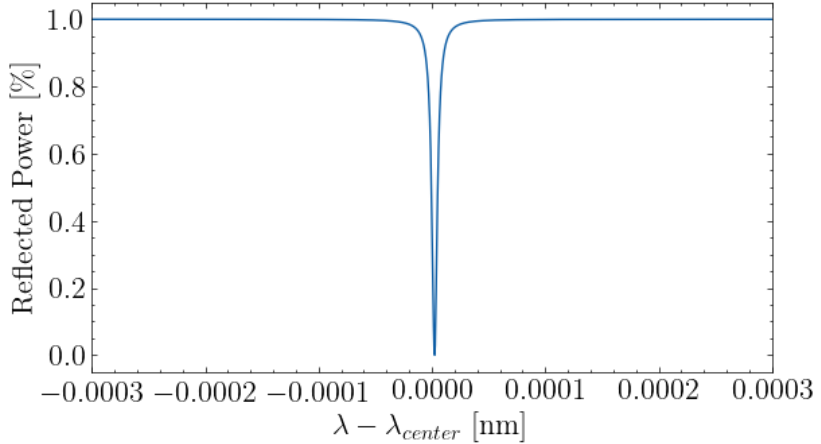


Figure 2.6: A closeup of Eq. 2.5 centered around a resonance point ($\lambda_{center} = 1143.074\,81\text{ nm}$, chosen arbitrarily as one of the resonance points within the working range of the laser diode), evaluated with the parameters $L = 15\text{ cm}$ with mirrors having $r = 99.8\%$. There is an obvious sharp dip in the reflected power around a single wavelength, indicating that theoretically, the incoming field couples almost completely to the cavity at this wavelength. These resonances repeat (infinitely) many times, spaced out by ν_{FSR} .

Another consideration when designing an optical resonator is the stability of the cavity. Given a cavity of length L and two mirrors with radius of curvature R_1 and R_2 , the stability parameters for each mirror can be defined as [33]:

$$g_1 = 1 - \frac{L}{R_1}, \quad g_2 = 1 - \frac{L}{R_2} \quad (2.9)$$

Stable cavities meet the criteria:

$$0 \leq g_1 g_2 \leq 1 \quad (2.10)$$

Confocal cavities are a cavity configuration where the focal point of one mirror is coincident with the plane of the other, i.e. $g_1 = g_2 = 0$, and are unique for their stability in the presence of small displacements and their suppression of longitudinal beam modes, leaving only the transverse Gaussian mode. Thus, a confocal cavity spacing, if possible, is desirable [33].

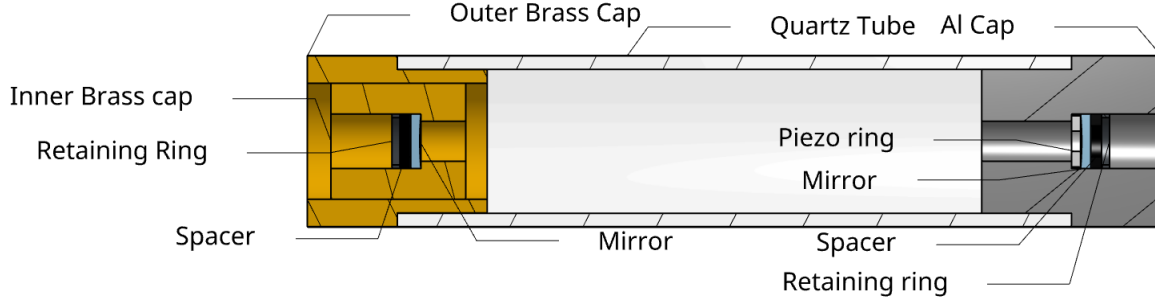


Figure 2.7: A cross sectional view of a 3D rendering of the FP cavity.

2.3.2 Construction

The cavity mirrors are two Layertec mirrors with a radius of curvature of 150 mm and a reflectivity of $> 99.8\%$ from 1030 - 1360 nm. Each mirror is housed in a metallic end cap, one made of brass and another of aluminum. The aluminum cap also houses a ring-shaped piezoelectric crystal, which upon the application of a voltage can actuate the position of the co-located mirror. Magnet-wire leads are attached to the two pads of the crystal using silver paint, coated in a layer of clear nail polish for mechanical stability. A quartz tube is used as a spacer to align and offset the two end caps by the necessary spacing required to establish a stable cavity. The spacing of the mirrors can be coarsely (compared to the piezo actuator) controlled by rotating the inner ring of the brass end cap, which consists of a threaded outer and inner ring to allow for the necessary linear translation. The construction of the cavity is depicted in Fig. 2.7.

The FP cavity itself rests on a pair of 3D printed spacers in a flange which holds it at a suitable height for optical routing, as shown in Fig. 2.8. The materials and geometry of the cavity were chosen to allow a configuration which counteracts the effects of thermal expansion at 300 K, resulting in a length stable against thermal fluctuations at around room temperature.

Specifically, using the coordinate system and the dimension labels as defined in Fig. 2.9(i.e. $x = 0$ at the center of the cavity), we have:

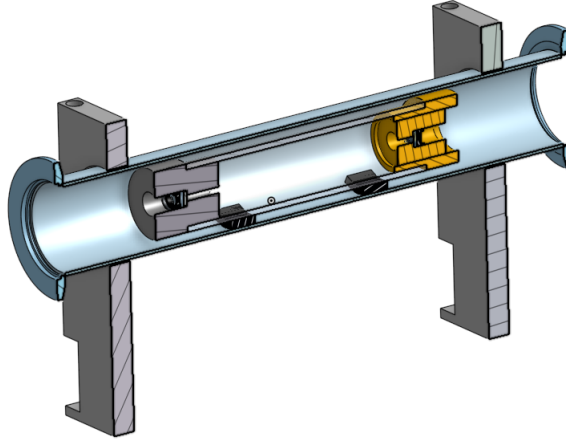


Figure 2.8: A cutaway showing the FP cavity assembly housed inside a metal flange.

$$\begin{aligned}\Delta X_1 &= \alpha_{quartz} (\Delta T) \frac{L}{2} \\ \Delta X_2 &= \alpha_{quartz} (\Delta T) \frac{-L}{2} \\ \Delta X_{piezo} &= \Delta X_1 + \alpha_{piezo} (\Delta T) (X_{piezo}) \\ \Delta X_{brass} &= \Delta X_2 + \alpha_{brass} (\Delta T) (X_{brass})\end{aligned}$$

In order for the cavity to remain the same length with temperature, the expansion effects must cancel out. Therefore:

$$\Delta X_{piezo} - \Delta X_{brass} = 0 \quad (2.11)$$

$$(\alpha_{quartz} L + \alpha_{piezo} X_{piezo} - \alpha_{brass} X_{brass}) \Delta T = 0 \quad (2.12)$$

Using $\alpha_{brass} = 19 \times 10^{-6} \text{ m K}^{-1}$, $\alpha_{quartz} = 5.5 \times 10^{-7} \text{ m K}^{-1}$ ², $\alpha_{piezo} \approx 5 \times 10^{-6} \text{ m K}^{-1}$ [34] and rearranging:

²https://www.engineeringtoolbox.com/linear-expansion-coefficients-d_95.html

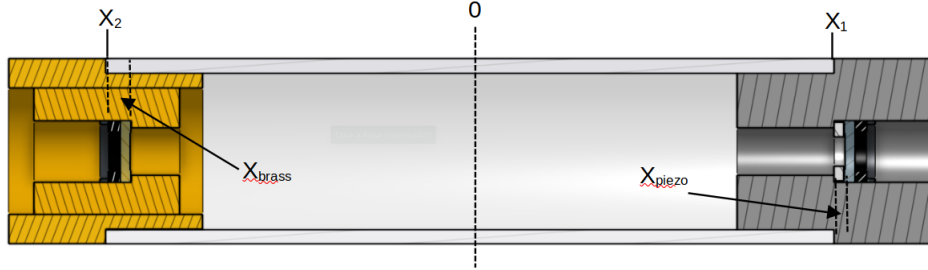


Figure 2.9: The FP cavity with dimensions of note given labels, and the center of the cavity being defined as $x = 0$.

$$X_{brass} = 9.8 \times 10^{-8} / 19 \times 10^{-6} = 4.86 \text{ mm} \quad (2.13)$$

Thus, in order to stabilize the cavity in the face of thermal fluctuations, the inner ring of the brass end cap needs to be moved 4.86 mm closer to the center of the cavity from the edge of the quartz tube. This comes at the cost of not being able to have a perfectly confocal cavity spacing, but is still a stable cavity configuration.

2.3.3 Optical Setup

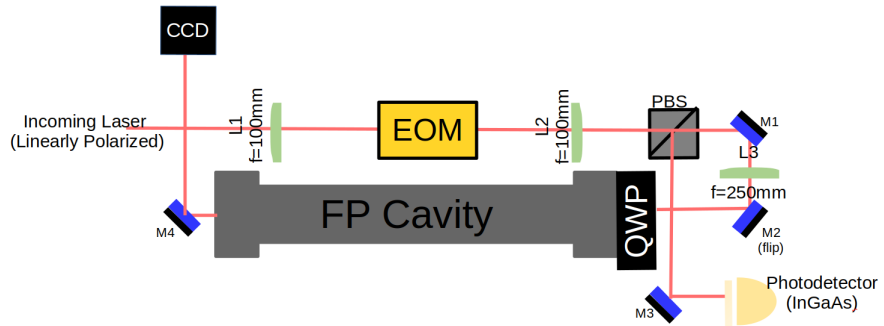


Figure 2.10: A diagram of the optical setup of the FP cavity component of the system, in isolation from the rest of the system for clarity.

The optical setup for the FP cavity is shown in Fig. 2.10. From the rest of the system, the beam enters the FP cavity first passing through a telescope of two lenses with a focal length of 100 mm, which serve to focus the beam in order to fully pass through the narrow aperture of the electro-optic modulator (EOM). Following this, the beam passes through a polarizing beam splitter (PBS), and fully transmits, as it arrives pre-polarized from the preceding section of the optical path (not shown). It then passes through two directing mirrors, with a focusing lens inbetween used to mode match the beam to the FP cavity. The beam then passes through a quarter-wave plate (QWP), circularly polarizing it, passes into the body of the flange housing the FP cavity, and meets the first mirror of the FP cavity itself. If the beam is not well aligned and/or the wavelength off resonance with the cavity, almost all of the beam is reflected, at which point it passes back through the QWP, returning it to a linear polarization, rotated by 90° from the original, such that upon returning to the PBS the beam is entirely reflected. This diverts light reflected off of the cavity towards a steering mirror and ultimately an InGaAs photodetector, which measures the intensity of the reflected signal, transducing optical power into a voltage.

If, on the other hand, the beam is well aligned to the cavity, and the wavelength is on resonance, a portion of the beam couples into the cavity, where it begins to circulate. Some of the circulating beam leaks out the front of the cavity, while the rest leaks out the back, where it can be measured using a photodetector or imaged using a CCD camera, as in this case.

2.3.4 Alignment

Alignment is first performed through the flange without the cavity present. To remove the cavity, remove QWP1 and flip down mirror M2. Then, gently pull on the leads to the BNC cable to remove the cavity. They are taped down to the outside of the cavity using kapton tape so it is safe to do so. Flipping M2 back up, use M2 to first align the beam to the center of the far side of the flange. Then use M1 to align the beam to the center of the near side of the flange. Repeat this process until the beam is centered at both ends. To aid in this centering, it may be useful to use one or both of the plastic flange caps which have had their centers punched out. These can be placed on either end of the flange, and used to check how close the beam is to the center. The punch may not be perfectly centered, so it may be useful to rotate the cap and observe the stationary part of the punched hole to see where the true center is. Once the beam is roughly centered to the flange, use M3 to direct the beam to the CCD1. Ensure that you can observe the beam using the camera.

Next, re-insert the FP cavity until the cap closest to the near side of the flange is aligned with the mark on the interior of the flange. This marks the correct spacing for the mode

matching lens to focus at the center of the cavity. Ensure that the cavity is sitting flat on the 3D printed spacers on the bottom of the flange, and is not tilted at any sort of angle. Using a small piece of IR card and a pair of forceps, ensure that the beam aligns roughly with the center of the mirror of the [FP](#) cavity. If it does not, adjust M1 until the beam is centered on the mirror. Then, use M2 to adjust the reflected beam until it is coincident with the incident beam. When properly aligned, the incident and reflected beams should be colinear up until the [PBS](#).

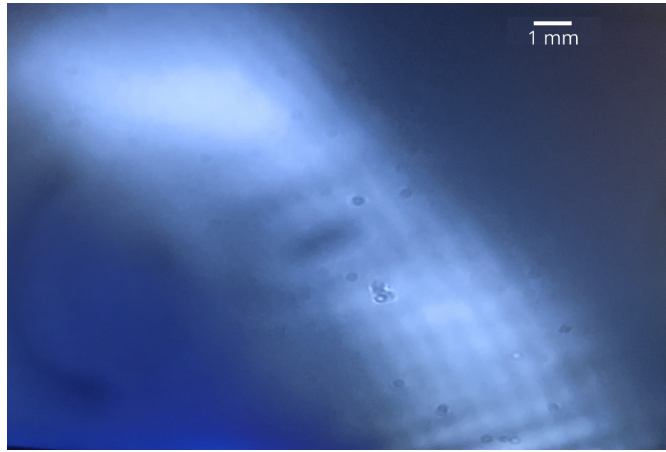


Figure 2.11: An example of the interference pattern generated by the cavity transmission, imaged by a CCD camera. Note that the interference pattern is spread out on a diagonal, indicating that adjustment of both the horizontal and vertical axis of the alignment mirrors is necessary to better align the cavity.

At this point, replace QWP1, and use M4 to direct the reflected beam into the photodetector. When sweeping the wavelength of the laser across a small range, or sweeping a voltage across the [FP](#) cavity's piezoe actuator, everything should be well aligned enough to see some small dips in the strength of the reflected signal. It should also be possible to observe a (possibly dim) interference pattern of light transmitted through the cavity using CCD1, an example of which is shown in Fig. 2.11. From here, the alignment can be refined by either attempting to deepen the resonance dips observed via the photodetector, or by trying to collapse the interference pattern seen in CCD1 into a single mode.

The method using CCD1 allows for visual feedback regarding the alignment of both axis of the alignment mirrors M1 and M2. To collapse the interference pattern seen via the camera, start by adjusting either the horizontal or vertical axis of both M1 and M2 at

the same time. Specifically, adjust one of the axis on M1 in either direction. Then adjust the same axis on M2 until the interference pattern is as condensed as possible (eventually it will start expanding again). If this newly observed pattern is smaller/brighter than previously observed, continue adjusting M1 in the same direction, followed by adjusting M2. If the observed interference pattern is dimmer than before, move the axis of M1 in the opposite direction, and use M2 to condense the spot size again. Once the interference pattern is collapsed along one axis, repeat the process with the other axis of both M1 and M2. Following this, you may need to re-adjust the initial axis to re-collapse it.

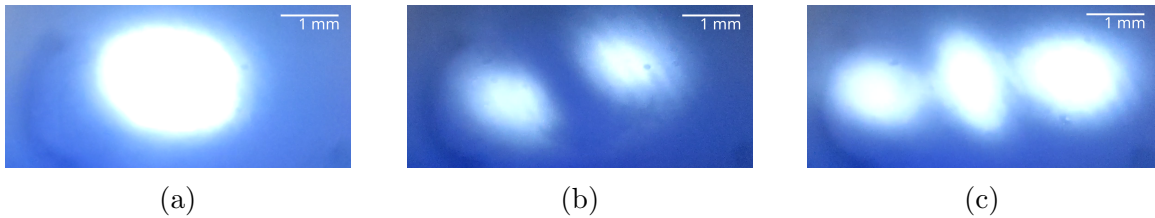


Figure 2.12: After further aligning the cavity, the transmission pattern should shrink, and begin to take the form of distinct Hermite-Gaussian modes, like the (a) 00, (b) 10, and (c) 20 modes shown here. Of note is that the modes of the cavity do not have to be exactly these modes to indicate good alignment (e.g. they could include 02 instead of 20), but should include at least the 00 mode.

Once the cavity has been well enough aligned, the interference pattern should collapse down and flash through recognizable Hermite-Gaussian modes (examples of which are depicted in Fig. 2.12) as the triangle wave sweeps the cavity across various resonance points. At this point, it may be possible to attempt to further optimize the alignment slightly by monitoring the dips in the reflected signal strength, and trying to maximize their depth.

2.4 Characterization

In order to characterize the FP cavity, it first needs to be well aligned. The quality of alignment can be determined by varying the wavelength of the laser by applying a periodic voltage to the diffraction grating piezo crystal and observing the signal of the power reflected off of the FP cavity by a photodetector, as well as observing the modes of the transmission though the cavity by CCD camera (or a simple index card). When scanning the wavelength of the laser, the largest dip in the reflected power (when the

wavelength is at resonance with the cavity) should have a depth of at least 70% of the off resonance reflected power. Additionally, the modes of the transmitted interference pattern should all be Hermite-Gaussian, with the 00 mode clearly visible at some point during the sweep. Together, these indicate that the input beam is aligned to the cavity.

Once the cavity is well aligned, the free spectral range of the cavity should be measured. This can be performed by tuning the wavelength of the laser (coarsely by turning the grating angle screw, then finely by adjusting the voltage of the grating piezoelectric crystal) to a wavelength corresponding to a 00 Hermite-Gaussian mode/deep resonance dip, and making note of that wavelength. Then, the wavelength needs to be increased or decreased (either is fine) until the next closest wavelength corresponding to another 00 Hermite-Gaussian mode is viewed. The difference between these two wavelengths (when converted to frequency) gives the [FSR](#) of the cavity, which can in turn be used to calculate the exact cavity length using Eq. [2.3](#). Additionally, by scanning the wavelength around a resonance, the linewidth of the resonance peak $\delta\nu$ can be experimentally measured from the [FWHM](#) of the peak, and then subsequently used to calculate the finesse F and quality factor Q , which can then be compared to the values predicted by Eqs. [2.7](#) and [2.8](#). Lastly, in order to facilitate wavelength scanning measurements incorporating the [FP](#) cavity, the laser wavelength needs to be able to be locked to the cavity for a period of at least two minutes.

2.5 Second Harmonic Generation

[second harmonic generation \(SHG\)](#) is a non-linear optical process in which the frequency of a photon interacting with non-linear crystals under the right conditions is doubled, producing light at twice the frequency of the fundamental laser light. This technique allows for the creation of high powered coherent laser light at wavelengths for which no commercial laser diode exists.

2.5.1 Theory of Second Harmonic Generation

Optical media under the illumination of a laser beam experience an electric field \mathbf{E} . If the medium has an average charge and current density of zero (i.e. it is a dielectric), then the presence of \mathbf{E} induces dipoles in the atoms and molecules, causing a position dependent polarization density, $\mathbf{P}(\mathbf{r})$. In general, \mathbf{P} is considered to be strictly proportional to \mathbf{E} , however, some materials exhibit a non-linear polarization response to an applied \mathbf{E} field, and \mathbf{P} has non-negligible higher order terms:

$$\mathbf{P} = \epsilon_0 \chi^{(1)} \cdot \mathbf{E} + \epsilon_0 \chi^{(2)} : \mathbf{E} \mathbf{E} + \dots \quad (2.14)$$

where $\text{chi}^{(i)} \forall i \geq 1$ are the i^{th} order electric susceptibilities, each of which take the form of an $i+1$ rank tensor, and the notation “ $:$ ” is used by Yamaguchi to denote the application of each of the vectors \mathbf{E} to $\chi^{(2)}$, a tensor of third rank, and results in a vector. This term $\chi^{(2)}$ is the term of interest, as it is what dictates the generation of the second harmonic light [35, 21].

The efficiency of second harmonic generation is governed by a condition called phase matching, which dictates that the strength of the second order term $\chi^{(2)}$ is maximal under the condition that the index of refraction in the non-linear medium is equivalent at both the fundamental ω and second harmonic 2ω frequencies[35]:

$$n(\omega) = n(2\omega) \quad (2.15)$$

There are two ways that this condition can be achieved in a birefringent crystal, depending on the specific material. So-called **critical phase matching** (**CPM**) can be achieved by carefully aligning the angle between the wave-vector and the optic axis of the crystal. **CPM** has the disadvantage that in some cases (specifically if the optical axis is not perpendicular to the wave vector), the birefringence of the crystal causes the incident beam to split along two polarization axes, creating a so-called "walk off effect" which leads to lower conversion efficiency[35].

The alternative to **CPM**, **non-critical phase matching** (**NCPM**), relies on the fact that the birefringent effect in some non-linear crystals varies as a function of temperature, allowing the phase matching condition to be satisfied with the wave vector perpendicular to the optical axis, producing no walk off simply by heating the non-linear crystal.

The single pass conversion efficiency η produced by a continuous wave Gaussian beam is given by[35, 36]:

$$\eta = \frac{P_{out}(2\omega)}{P_{out}^2(\omega)} = 16\pi^2 \frac{d_{\text{eff}}^2 L}{\epsilon_0 c n^2 \lambda_0^3} h(B, \xi) \quad (2.16)$$

where d_{eff}^2 is the crystal's non-linear coefficient, L is the crystal length, ϵ_0 is the vacuum permittivity, c is the speed of light, n is the refractive index of the crystal, λ_0 is the fundamental wavelength, and $h(B, \xi)$ is the Boyd Kleinmann focusing factor, which attains a maximum value of slightly greater than 1 under the condition that $B = 0$ (always the

case in NCPM) and $\xi = 2.84$, which is dictated by the beam waist, and can be designed for when constructing an enhancement cavity[37]. Given a $L = 20\text{ mm}$ Lithium triborate LiB_3O_5 (LBO) crystal and meeting the non-critical phase matching condition, it is possible to achieve:

$$\eta_{shg} = 2.364 \times 10^{-4} \text{ W}^{-1} \quad (2.17)$$

Through the use of ABCD matrices, a bowtie cavity meeting the desired beam waist requirements can be designed in order to enhance the SHG conversion efficiency by circulating the beam through the non-linear crystal multiple times [35].

2.5.2 Components and Optical setup

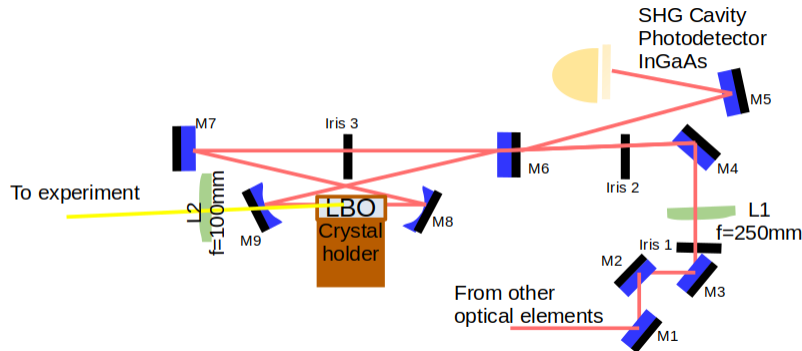


Figure 2.13: A diagram of the optical setup of the cavity enhanced SHG component of the system, in isolation from the rest of the system for clarity.

The optical layout for the SHG cavity is shown in Fig 2.13. Several mirrors (M1, 2, 3, & 4) direct the laser light from the rest of the optical setup towards the bowtie cavity itself, with a lens L1 focusing the light at the center of the long arm of the cavity to provide mode-matching. The cavity itself is comprised of four special mirrors. The first, M6 is a planar mirror with a 98.5% reflective coating for 1150 nm, and allows some of the incoming light to couple into the cavity. The next mirror, M7, is also a planar mirror, but is coated for 99.8% reflectivity at 1150 nm. The two mirrors surrounding the LBO crystal are both plano-concave, with a radius of curvature of 50 nm, and are 99.8% reflective at 1150 nm, and AR coated for 575 nm. A plano-convex lens is used on the output light of the cavity

to re-collimate it. Lastly, M5 and an InGaAs **photodetector (PD)** are used to measure the light reflected off of the cavity, and are used to generate an electrical signal used for locking the cavity.

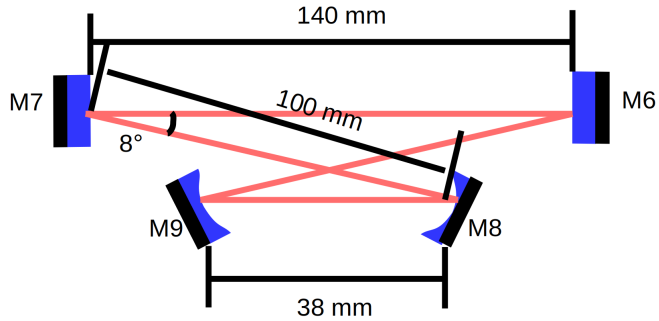


Figure 2.14: The dimensions of the bowtie cavity. Drawing is not to scale.

As determined using ABCD matrices to solve for the cavity parameters, the distance between mirror M6 and M7 (the long arm of the cavity) is 140 mm, the distance between the short arm of the cavity (M8 and M9) is 38 mm, and the perpendicular distance between each arm is 13.91 mm. This makes the straight-line distance between M7 and M8 100 mm, at an 8° angle from the beam between M6 and M7, as shown in Fig.

Figure 2.15 shows the assembly responsible for the heating and positioning of the non-linear crystal. The $2 \times 2 \times 20$ mm LBO crystal itself is wrapped in aluminum foil and cradled in a machined copper holder, with a 3D printed wedge holding it in place. The copper holder is epoxied to a 40×40 mm Peltier TEC unit, which is in turn epoxied to a 3D printed plate. This plate couples to another plate which acts as an adapter for a rotational stage, with another 3D printed part adapting that to an XYZ-positioning stage (only the top of which is shown in the figure). The resulting assembly allows for precise rotation/positioning of the crystal.

2.5.3 Alignment

Cavity alignment is performed in multiple stages. First, the beam is roughly aligned to the cavity using mirrors M2, 3, & 4 and a series of three irises which have post collars limiting them to the same height. Alignment is performed starting with mirror M2, which is used to align the beam to the center of first iris. Mirror M3 is then used to align the

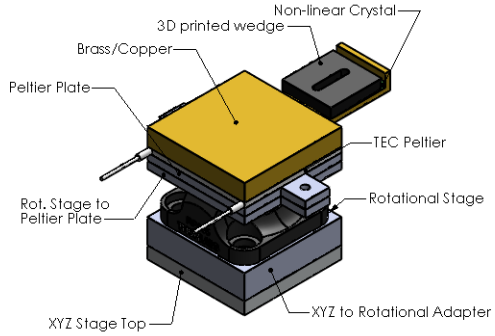


Figure 2.15: The crystal holder assembly. The crystal is heated to the non-critical phase matching temperature using a TEC, whose heat is conducted by a machined copper holder. Other components are used to mate the TEC/Copper arm to a 360° rotational stage, which is then mounted on an xyz-positioning stage, of which only the very top is shown in this figure.

beam to the second iris, and mirror M4 used to align to the third iris. Then, the process is repeated again, starting from the beginning with mirror M2, since the adjustment of mirror M3 to align with the second iris may have slightly changed the alignment relative to the first iris. Iterations of this procedure are repeated as many times as necessary until the beam deviation upon each iteration is negligible. Also, it may be useful to slightly miss-align the beam to the second and third iris. Specifically, aligning the beam slightly (3-4 mm) right of center (towards the exterior of the cavity) can make it easier to align mirror M7 to mirror M8, as hitting this planar mirror slightly off-center is harmless and can give an angle to mirror M8 that is less likely to clip on mirror M9.

When aligning the mirrors of the bowtie cavity, remove the third iris and begin with mirror M7, skipping mirror M6 for now. Mirror M7 should be aligned such that the laser hits the center of mirror M8 without clipping on mirror M9 or the crystal holder. Mirror M8 should be aligned to direct the beam to the center of mirror M9 when the beam passes through the LBO crystal, which may require a slightly different alignment than when the crystal is not in place. Next, mirror M9 should be aligned to reflect the beam back at mirror M6 in the exact spot that the beam passes the plane of the mirror on the interior of the cavity. Lastly, mirror M6 should be adjusted to direct the beam from the first circulation through the cavity to the point on mirror M7 that the original beam hits. Using an IR card, it is possible to distinguish the original and first pass beams, because when blocking the original beam to view it with the card, the first pass beam will disappear. Once the

first pass beam is aligned well enough, it may be possible to see second, third, or forth circulation beams by moving the IR card in and out to progressively block and unblock each n^{th} beam circulation.

At this point, the cavity alignment needs to be fine tuned so that as many circulations through the cavity as possible overlap. This fine tuning is usually performed by adjusting mirrors 6 and 9, keeping mirrors M7 and M8 fixed. First, position the IR card in front of mirror M6, and adjust mirror M9 to align as many circulations with the incoming original beam as possible. At some point, it will be impossible to improve the alignment any further (the beams will not converge no matter what adjustments to mirror 9 are made) and mirror M6 should be adjusted to align the beam paths at mirror M7.

While adjusting mirror M6, mirror M5 should also be adjusted to ensure that the cavity reflection is directed at the sensor on the InGaAs photodetector. Once the cavity is aligned well enough, small dips in the reflection of the cavity should be observed when sweeping a voltage across the mirror M7 piezo actuator. When this is the case, it is possible to fine tune the alignment of the cavity by adjusting the same axes (either horizontal or vertical alignment) of both mirrors M6 and M9 simultaneously, with the figure of merit being the depth of the dip in reflected intensity, as these indicate light coupling to the cavity.

Another way to fine tune the alignment of the cavity is to use a CDD camera to image the interference pattern (the light of each pass through the cavity can interfere constructively and destructively with the rest of the light circulating in the cavity) of the cavity transmission, similar to the [FP](#) cavity alignment. As with the [FP](#) cavity, the goal is to adjust one axis of both mirror M6 and M9 at a time in order to collapse the interference pattern along one axis, and then adjust the other axis of both mirrors to collapse the interference pattern along the other axis. The final transmission pattern should be the 00 Hermite-Gaussian mode. As the voltage sweeps, other modes may briefly appear, but the single mode corresponds to the deepest resonant peak visible.

As a final note regarding alignment, this cavity used $\varnothing 1/2"$ mirrors. While these mirrors provide larger targets for alignment, it may be more practical to use smaller optical components if possible. Namely, the path from mirror M7 to M8 can easily clip on mirror M9 if not carefully aligned. Because of this, smaller mirrors might make alignment easier despite the decrease in reflective area, and might also allow for the output collimation lens L2 to be positioned better.

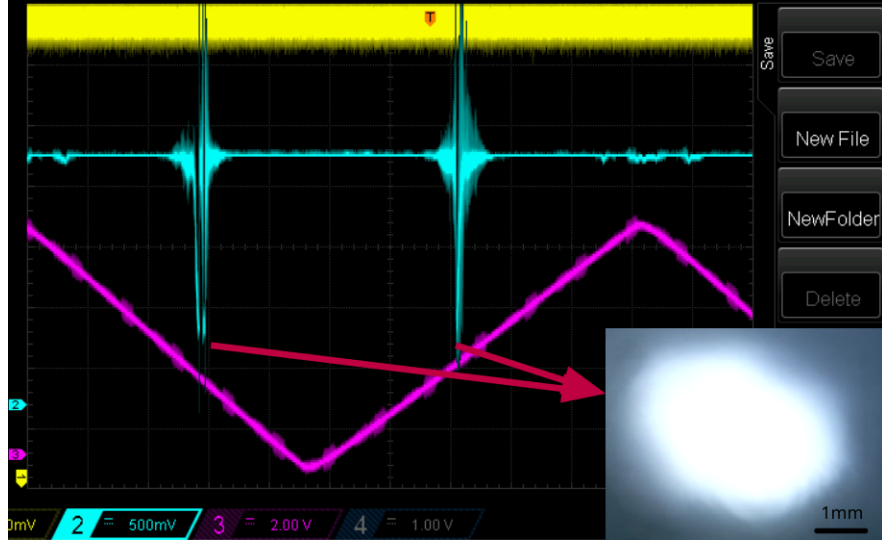


Figure 2.16: An oscilloscope trace showing the strength of the signal reflected off of the cavity as measured by a photodetector (blue trace) when sweeping a triangle wave across the piezo of mirror M7 (purple trace). An image of the resulting cavity transmittance corresponding to the deepest peaks is inset.

2.5.4 Locking

Locking of the cavity is performed using the [PDH](#) technique, as with the [FP](#) cavity. In the case of the [SHG](#) cavity, a Moku:Lab running the laser lock box instrument is used, with the AFG1062 [arbitrary function generator \(AFG\)](#) used as an external oscillator to supply the phase modulation used in [PDH](#), as opposed to use the Moku's internal local oscillator.

The intended way to lock using the laser lock box instrument is depicted in Fig. 3 of [38], which shows the laser lock box instrument interface. In the top panel, a block diagram of the instrument is shown, which allows for graphical editing of block parameters, as well as the ability to turn outputs on and off and set points to measure a signal trace using the oscilloscope in the bottom panel. In the figure, the bottom panel is currently in locking mode, which automatically moves one of the traces to the RF mixer output and allows the user to select a zero crossing of the error signal to lock to. When scanning a voltage across the cavity, it is possible to tap on the crosshairs of the zero crossings in the error signal (Trace A in Fig. 3 of [38]) to attempt to lock the PID to that point. In the case of the figure, the zero crossing in the center would be the desired choice, as this is at the

center of the **PDH** error signal. In practice, this was found not to work well, both due to a much noisier error signal, as well as difficulty in using the tap based interface. For example, zooming in and out is difficult, and frequently trying to tap on zero crossing can lead to selecting another trace if it is active.

By closing the oscilloscope using the 'x' in the upper left of the panel, one will be presented with the view depicted in Fig. 1 of [38]. It was found that in practice, it was easier to get a lock by first starting a scan with the "Scan On" button, then engaging the lock with the engage/disengage lock button, and finally, stopping the scan. Occasionally, the Moku will lock to one of the smaller multi-mode peaks when using this method. In that case, it is possible to adjust the offset of the fast controller branch up or down, then repeat the procedure. This method is not ideal but can be helpful for being able to lock to the correct peak.

The Moku interface also has a number of control blocks that allow for parameters to be adjusted via a graphical interface, for example, the PID controller, as shown in Fig. 4 of [38]. For the PID controller, a proportional gain of 0 dB, integrator corner frequency of 125 kHz, and integrator saturation of 20 dB were found to work the best for locking stability, although overall there was difficulty encountered in getting the Moku to successfully lock the cavity for periods longer than 10 seconds. For the lowpass filter, a corner frequency of 9 MHz (close to the **PDH** phase modulation frequency) worked well.

As mentioned above, the Moku has some issues regarding locking stability. Namely, the output voltage of the Moku is at maximum 2 V peak to peak, which, even after passing through the HV amplifier, is not sufficient to cover the **FSR** of the **SHG** cavity. This means that at some wavelengths, the single mode resonances of the cavity are inaccessible, and at the wavelengths that they are, locking can be unstable due to the limited scanning range available.

2.6 Characterization

Full characterization of the **SHG** cavity should involve the following: The cavity should be well aligned, such that the main resonance dip viewed when scanning a triangle wave across the cavity piezo has a depth of at least 70% of the off-resonance reflected power. Going hand in hand with this, the transmission modes visible when sweeping a voltage across the piezo should all be Hermite-Gaussian, with the 00 mode specifically being visible at some point during the sweep. Both of these factors indicate good alignment to the cavity, which leads to better coupling of the input power at resonance, and consequently higher output

power. When the cavity is locked, the transmission of the cavity should appear to be in the 00 Hermite-Gaussian mode when viewed with the CCD camera. If the mode is not 00, then the cavity is locked to a resonance peak corresponding to another (less efficient) mode. In order to facilitate scanning the laser wavelength to make a measurement, the cavity should be able to be locked for at least 2 minutes at a time. Lastly, when locked, the output power should be on the order of the theoretically predicted output power obtained by the product of the input power and the theoretically calculated conversion efficiency.

2.7 Electronic Control and Laser Stabilization

2.7.1 The Pound–Drever–Hall Laser Stabilization Method

As discussed in the [FP](#) cavity section, the primary indicator for determining whether or not laser light is on resonance with a cavity is to measure the power reflected off of the cavity. Ideally one could use the measured reflected power to determine when the laser is off resonance, and apply electronic feedback (either to the cavity, or some aspect of the laser) to restore resonance. Unfortunately for this particular application, the resonance dip signal is symmetric, so it can be used to determine whether a cavity is on or off resonance, but not which direction to adjust the frequency of the laser/cavity dimension to return to resonance. For example, a 5% increase in reflected power could be the result of moving to either a higher or lower wavelength in Fig. [2.6](#). In addition, this sort of feedback is sensitive to any changes in the intensity of the light itself. The desired error correcting information is, however, encoded in the slope of the resonance dip, so we can use the derivative of the reflectance signal to define an appropriately signed error signal [\[32\]](#). The [Pound–Drever–Hall \(PDH\)](#) method provides a way to access this information and use it in a feedback control system to provide electronic cavity/laser stabilization.

The following derivation mostly follows [\[32\]](#). Modulating the incident light sinusoidally with frequency Ω and modulation depth β ($\beta \sin \Omega t$) gives:

$$E_{inc} = E_0 e^{i(\omega t + \beta \sin \Omega t)} \quad (2.18)$$

which can be rewritten using the small angle approximation to:

$$E_{inc} \approx E_0 (1 + i\beta \sin \Omega t) e^{i\omega t} = E_0 (e^{i\omega t} + (\beta/2) (e^{i(\omega+\Omega)t} - e^{-i(\omega-\Omega)t})) \quad (2.19)$$

showing the clear presence of two side-bands at $\omega \pm \Omega$. Applying the transfer function $H(\omega)$ gives:

$$E_{ref} = E_0 (H(\omega) e^{i\omega t} + (\beta/2) (H(\omega + \Omega) e^{i(\omega+\Omega)t} - H(\omega - \Omega) e^{-i(\omega-\Omega)t})) \quad (2.20)$$

Usually a photodetector measures the reflected power $P_{ref} = |E_{ref}|^2$, which can be put in the following form with some rearrangement:

$$\begin{aligned} P_{ref} &= P_0 |H(\omega)|^2 + P_0 \frac{\beta^2}{4} (|H(\omega + \Omega)|^2 + |H(\omega - \Omega)|^2) + \\ &\quad P_0 \beta (\text{Re}[\varepsilon(\omega)] \cos \Omega t + \text{Im}[\varepsilon(\omega)] \sin \Omega t) + (2\Omega \text{terms}) \end{aligned} \quad (2.21)$$

with

$$\varepsilon(\omega) = H(\omega) H^*(\omega + \Omega) - H^*(\omega) H(\omega - \Omega) \quad (2.22)$$

In practice, $\varepsilon(\omega)$ is the term we are interested in, as it is the term oscillating at the modulation frequency, and will allow us to measure the phase. By mixing the signal from the photodetector with a 90° phase shifted version of the original modulation signal and low-pass filtering (since $\omega \gg \Omega$), it is possible to remove the non- $\varepsilon(\omega)$ terms. Assuming a high enough modulation frequency, the modulation side-bands are outside the resonance region of the cavity and are therefore fully reflected (i.e. $H(\omega \pm \Omega) \approx -1$), then:

$$H(\omega) H^*(\omega + \Omega) - H^*(\omega) H(\omega - \Omega) \approx -i2 \text{Im}[H(\omega)] \quad (2.23)$$

This at last, gives the error signal:

$$\epsilon(\omega) \approx P_0 \beta (\text{Re}[-i2 \text{Im}[H(\omega)]] + \text{Im}[-i2 \text{Im}[H(\omega)]]) = -2P_0 \beta \text{Im}[H(\omega)] \quad (2.24)$$

which can been seen in Fig. 2.17 evaluated for the parameters given by the FP cavity at the resonance point depicted in Fig. 2.6, with a modulation frequency of 9.6 MHz. The region of interest in this case is the linear portion in the very center of the error signal, which can be used fed into a control system (for example, a PID controller) and used to provide correcting feedback to the system.

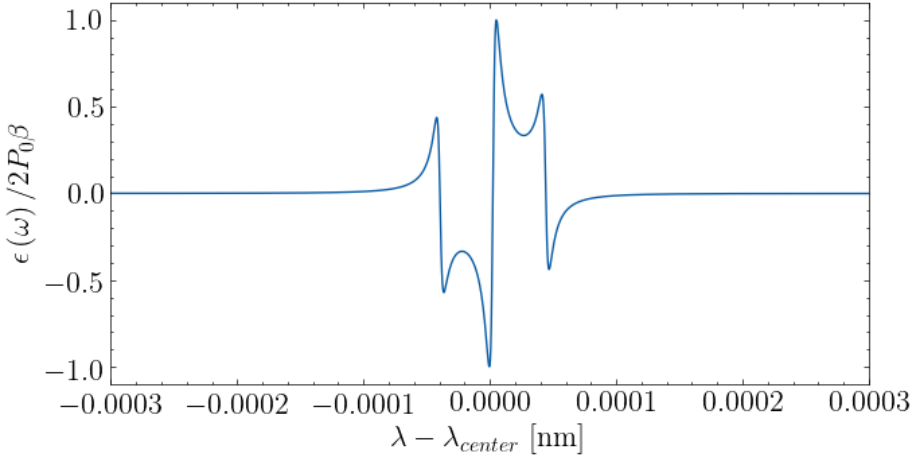


Figure 2.17: The error signal obtained via the [PDH](#) method, simulated for a [FP](#) cavity with the parameters $L = 15$ cm and mirrors of $r = 99.8\%$, with a modulation frequency of 9.6 MHz around a resonance point at $\lambda_{center} = 1143.074\,81$ nm. Typically, the error signal would be considered in terms of frequency, but it was kept in the wavelength domain for the sake of comparison to Fig. 2.6.

2.7.2 Signal Routing

Figure 2.18 represents the various devices and their connections in block diagram form, which are described in detail below.

A Tektronix AFG1062 [AFG](#) is used to generate two sinusoidal dithering signals of approximately (the exact frequency can vary slightly) 9.6 MHz. The signal on Channel 1 is immediately split using a t-junction, with one part of the signal acting as input to an [EOM](#) which modulates the phase of the laser light directed towards the [FP](#) cavity. The other portion of the signal is passed through a 20 dB attenuator, before being fed into one of the inputs of a Mini Circuits ZRPD-1+ phase detector. The other input to the phase detector originates from a Thorlabs PDA20CD2 InGaAs amplified photodetector, which measures the light reflected from the [FP](#) cavity. The output of the photodetector first passes through the RF + DC terminal of a Mini Circuits ZFBT-4R2GW+ bias tee. The DC terminal of the bias tee is terminated with a 50Ω plug, while the RF terminal is passed as the input to the RF mixer, effectively filtering out the DC component of the signal. The output of the RF mixer is the [PDH](#) error signal, and is passed as input to the UQML laser controller box. In the laser controller box, the error signal is passed into a two

branch PID controller. One branch of the controller, the "fast" branch produces a signal which is then passed to the current source for the laser diode (another circuit in the same UQML laser controller box). The second branch of the PID, the "slow" branch produces a signal between 0-5 V which is fed to one of three channels of a PiezoDrive PDu150 HV amplifier, with a gain of 20 V/V. The amplified signal is then applied to a piezoelectric crystal which actuates the position of the grating, thereby modulating the frequency of the laser. The UQML laser lock box also supports application of an arbitrary waveform (provided by an external source, in this case a Newark GFG-8215A [function generator \(FG\)](#) used to produce a triangle wave) on the same piezo crystal modulation channel, with the option control the peak to peak voltage of the swept waveform, and apply a 0-5 V DC offset.

Much like the first channel of the Tektronix [AFC](#), the dithering signal generated by the second channel is also immediately split, with one branch being similarly attenuated by 20 dB before entering the second input channel of a Liquid Instruments Moku Lab. The other branch of the dithering signal is directed to the RF port of another Mini Circuits bias tee. The DC port of this bias tee is connected to the first output channel of the Moku lab (which can produce a 2 V peak-to-peak output signal), with the RF + DC port acting as input to the first channel of the HV amplifier, the output of which is applied to a piezoelectric crystal o-ring on which one mirror of the [SHG](#) cavity is mounted. In this way, the bias tee is essentially combining the control and phase dithering signal into one, which is then applied to the [SHG](#) cavity to enable [PDH](#) method stabilization. The first input to the Moku Lab, which is generating the control signal, comes from another Thorlabs InGaAs photodetector, which in this case measures the light reflected from the [SHG](#) cavity. This signal is fed directly into the Moku, as the DC bias removal, RF mixing, and PID signal processing is all performed internally. Like the UQML laser lock box, the Moku Lab has both "fast" and "slow" PID control branches, but in the case of the [SHG](#) cavity, only the slow branch is used, to modulate the voltage applied to the piezo crystal on which the mirror is mounted, as there is no other cavity input to modulate in this instance. The Moku Lab can also be used to apply a triangle, saw-tooth, or sine wave sweep as output instead of a control signal.

The last channel of the HV amplifier, Channel 2, receives input from one of the [digital to analog converter \(DAC\)](#) channels available on a Measurement Computing USB-1608GX-2AO, which allows for the computer control of an arbitrary analog output with 16 bits of resolution. The amplified signal is then applied across another piezoelectric o-ring, this time installed inside one end cap of the [FP](#) cavity, allowing for scanning of the cavity resonant frequency across part of the free spectral range of the cavity.

The signal routing described above represents an ideal case. In the experimental results

discussed in Chapter 3, some modifications were made, which are described there.

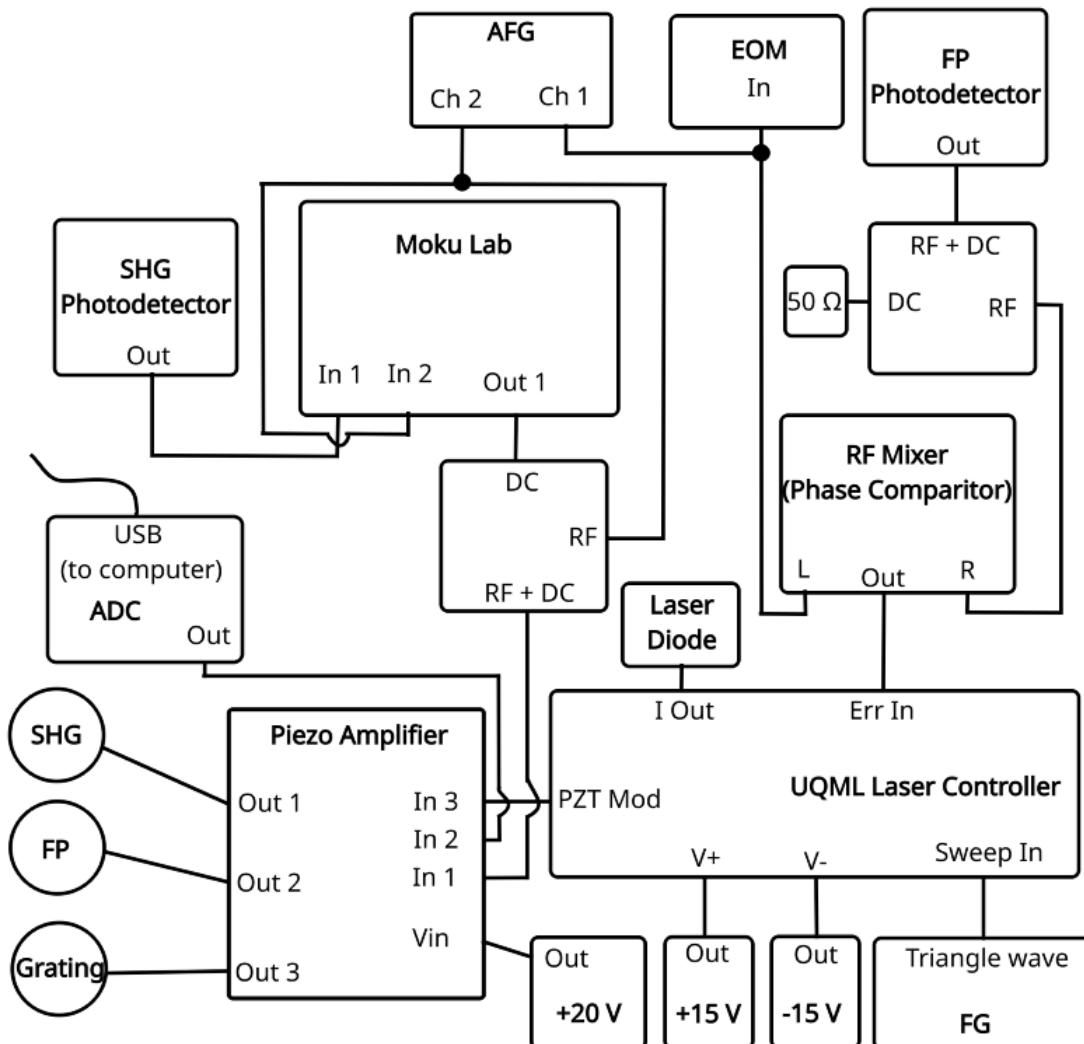


Figure 2.18: A block diagram representing the interconnection of the various signal paths and forms of electronic control.

Chapter 3

Sample Measurement and Analysis

This chapter describes an experiment making use of the laser system described in the previous chapter, in which the transmission of the SHG laser light through a Cu₂O sample cooled to 100 K is observed while varying the wavelength of the light. These transmission measurements are then analyzed to produce a high resolution spectral scan across the $n = 4$ and $n = 5$ yellow P-exciton resonance peaks. After converting from transmittance to absorbance, the parameters of each resonance peak are determined by fitting Toyozawa's asymmetric Lorentzian function (Eq. 1.3) to each peak, which allows for further fitting of Eq. 1.1 to extract the bandgap energy E_g and Rydberg energy R_y . The values for these parameters obtained by fitting the high resolution spectral scan are then compared to the values obtained by performing similar feature extraction on an absorption spectrum calculated from the transmission spectrum of a broadband white light source captured by a spectrometer at the time of the high resolution scan, and to values obtained during a previous study using similar white light transmission spectroscopy [2].

3.1 Contribution Statements

Besides the laser system itself, a number of devices used in the experiment described below were set up by others. Specifically, Prof. Na Young Kim, HeeBong Yang and Dr. Daniel Kang setup the spectrometer, wavemeter, and installed the cryostat. The design and mounting of the sample holder in the cryostat were performed by Dr. Daniel Kang and Prof. Na Young Kim. Lastly, the Cu₂O sample used was provided courtesy of Prof. Yoshioka's group, and was polished by Prof. Na Young Kim.

3.2 Experimental Setup

For the experimental results presented below, unfortunately neither the [FP](#) cavity nor the [SHG](#) system were used at their full potential. In the case of the [FP](#) cavity, it was, at the time of the experiment, unaligned as a result of a change made along the optical path closer to the laser source, meaning that the laser was not able to be locked to it, and was therefore unused. The [SHG](#) cavity was aligned, but locking proved to be unstable (lasting on the order of < 10 s). Additionally with an input power of 40 mW in the fundamental frequency to the [SHG](#) cavity, output [SHG](#) light with a power of less than 10 μ W was produced when locked, which was not observable using the photodetector on the transmission side of the sample. Instead, a 10 Hz triangle wave (40 V peak to peak) was used to sweep the cavity. This resulted in brief pulses of bright yellow light with a peak power of around 10 μ W (which may be instantaneously higher, and partially diminished by the power meter's response time), produced in the brief moment that the cavity was on resonance.

The pulses of light produced by the [SHG](#) bowtie cavity were directed over free-space via mirrors towards a Cryo Industries of America 2 K cryostat, in which the Cu₂O sample was mounted. The optical setup used to illuminate the sample and analyze the transmission is shown in Fig. 3.1. The incoming [SHG](#) laser light first hits a beam sampler, which samples about 10 % of the power of the incoming light, directing it towards a Si variable gain amplified photodetector [PD1](#). The remaining 90% of the beam passes through the sampler, hitting M1, which is used to select between the white light or yellow laser light source. From this flip mirror on, the two light sources follow the same path, traveling through a plano-convex lens L1 ([AR](#) coated for the visible spectrum) which focuses the light on the sample mounted in the cryostat, after which the light is re-collimated using another plano-convex lens L2. From here, the two different lights have their paths diverge again, as determined by another flip mounted mirror M2, which is used to direct the yellow laser light to another Si photodetector [PD2](#), and the broadband white light to a Princeton Instruments HRS-750 Spectrometer.

The spectrometer was used to measure the spectrum of the white light both transmitted though the sample, and through a hole in the sample holder (used to obtain the raw white light spectrum for normalization). [PD1](#) was used to measure the intensity of the incoming yellow laser light, which allowed the light transmitted through the sample, measured by [PD2](#) to be normalized, as the intensity of the [SHG](#) light was highly variable due to the aforementioned sweeping over bowtie cavity resonance points. Both [PDs](#) transduced the power of the light incident on them into a voltage which was sampled using two [analog to digital converter \(ADC\)](#) channels of a Measurement Computing USB-1608GX-2AO. The wavelength of the fundamental (non-[SHG](#)) laser light was continuously monitored

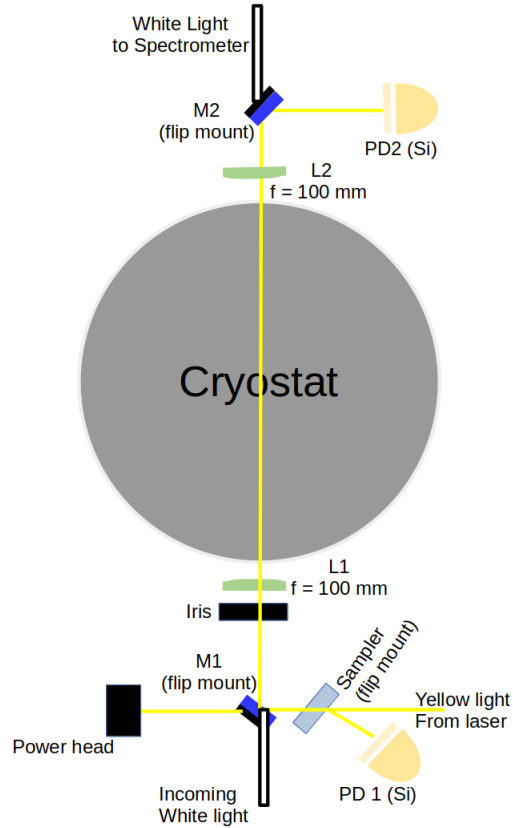


Figure 3.1: A diagram of the optical setup used to illuminate the Cu_2O sample with both the yellow SHG laser light and a white light source.

using an Angstrom WS-6 Wavelength meter.

In the case of the yellow SHG laser light, the wavelength of the light was varied in order to create a high resolution scan of the transmission of the sample over a range of wavelengths. In principle, the scanning of the laser wavelength would be accomplished by locking the laser to the FP cavity, and applying a voltage to the piezoelectric crystal inside the FP cavity using a DAC channel of the USB-1608X-2AO to vary the resonant frequency of the FP cavity. In practice, since the FP cavity was not used in this experiment, the wavelength of the light was changed by bypassing the PID functionality of the laser lock box and using the voltage offset knob to directly vary the voltage applied to the piezo crystal mounted behind the diffraction grating. In order to facilitate smooth, continuous,

and electronic control of this applied voltage, with minimal modification to the laser lock box, the very ad hoc solution of mechanically coupling the voltage offset knob to a stepper motor using a timing belt and a 3D printed shroud was devised. This method allowed for a continuous scan of a wavelength range about 0.1 nm wide in the yellow light, or 0.2 nm in the fundamental laser wavelength, which is halved by **SHG**.

Since the **ECDL** utilizes a Littrow configuration, varying the wavelength of the light has the effect of changing the outgoing angle of the laser light as well. This, consequently, results in the strength of the fiber couple (Fig. 2.5), and therefore the strength of the light incident on the **SHG** cavity, varying throughout a sweep. To mitigate this effect as much as possible, the fiber couple was typically optimized for a wavelength at the center of the wavelength range being scanned. In order to sweep ranges larger than 0.1 nm, a set screw was used to manually adjust the grating angle. Due to the aforementioned coupling efficiency effect, an overlap of around 0.05 nm between each sweep was chosen.

Using this experimental setup, the Cu₂O sample mounted in the cryostat was cooled down to 100 K using liquid He. White light transmission spectroscopy was used to verify the spectral position of the visible yellow P-exciton peaks at this temperature, after which a high resolution scan of the $n = 4, 5$ peaks (575 nm to 576.5 nm) was performed using the yellow **SHG** light pulses by performing 0.1 nm scans in 0.05 nm increments, until the entire region of interest was scanned. The data from the measurement analyzed in the next section was taken as previously described with the assistance of Marcel Robitaille.

3.3 Data Analysis

Due to the pulsed nature of the laser light, a fair amount of post-processing is required to convert the raw data into a usable spectrum. Figure 3.2 shows the raw data obtained as the result of a single scan over a range of 1152.85 nm to 1153.07 nm (fundamental wavelength), consisting of sampled voltage from two imaging **PDs** over a period of about 60 s. Not shown, but also measured is the wavelength of the fundamental laser wavelength, allowing each point of data to be associated to a particular wavelength of light.

Focusing perspective on the region around 10 s in Fig. 3.3, several details become apparent. First, the peaks visible in Fig. 3.2 are in fact clusters of narrow peaks of varying heights. These peaks are produced by the sweeping of the bowtie cavity dimensions by the 10 Hz triangle wave resulting in brief periods of resonance, resulting in typically single mode **SHG** generation. The smaller peaks can be attributed to the cavity passing resonance points which occasionally allow for two, three, or more mode **SHG** generation, which are

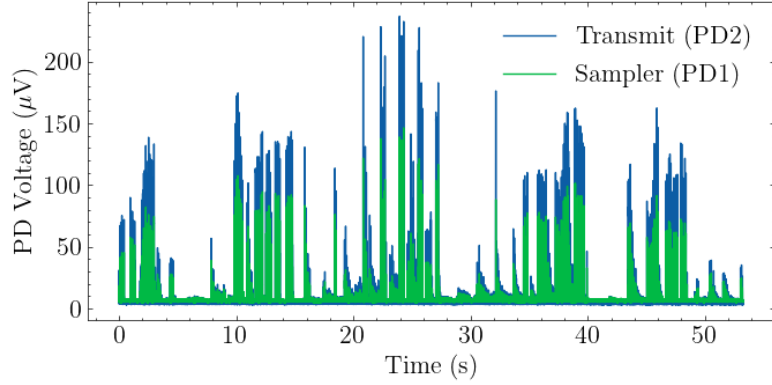


Figure 3.2: Voltage signals sampled by [ADC](#) from the two imaging [PDs](#), depicting one offset-knob rotation based scan from 1152.85 nm to 1153.07 nm ($\delta_{\text{scan}} \approx 0.2 \text{ nm}$). Each point has an associated wavelength measurement, indicating the fundamental laser's wavelength at that point in time. Variation in the height of the signal is caused by two factors. Varying the wavelength changes the output angle of the laser from the laser cage, which changes the strength of the laser's coupling to the fiber couple (C1, [2.5](#)). The other cause of the variation is a change in the resonant characteristics of the cavity over time. This can be caused by a number of factors including temperature variation and air currents. For some conditions, the cavity parameters change significantly enough that the 2 V_{pp} output of the moku (amplified to 40 V_{pp} by the HV amplifier) is insufficient to reach a resonance point.

weaker in intensity than the single mode. The other notable observation to be made from Fig. [3.3](#) is the presence of a small DC bias which is different in both signals. This bias can be attributed to the inherent bias introduced into the signal by the amplifier in the [PD](#) and varies at different gain settings, and can also be affected by small differences in ambient light conditions.

Zooming in one last time, the shape of an individual peak can be observed in Fig. [3.4](#). The first steps of analysis have also been performed, namely the aforementioned DC bias has been removed by subtracting the average of each signal from itself. In addition, the local maximum of each signal has been identified and marked. By comparing the height of the peak measured by the transmission [PD](#) to the strength measured by the sampler [PD](#), a normalized value for the transmission can be obtained, which, combined with the known wavelength of the light producing that peak, can be used to generate a single point of a transmission scan of the yellow P-exciton spectrum.

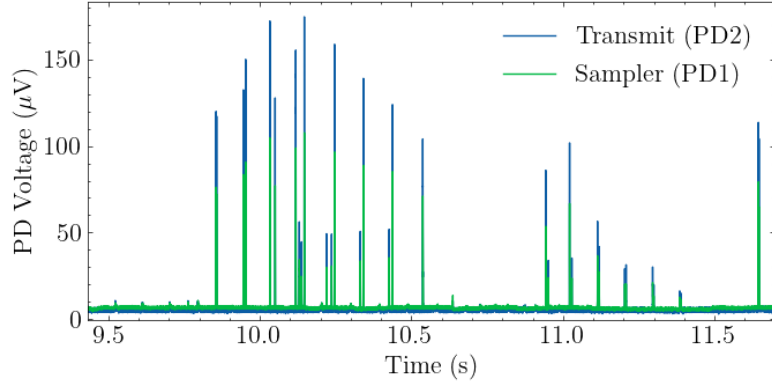


Figure 3.3: A closeup of the 10 s region from 3.2, revealing that the areas of higher voltage signal are actually clusters of very narrow voltage spikes. The main spikes are all spaced approximately 0.1 s apart, corresponding to resonances crossed by the 10 Hz triangle wave. Medium sized peaks and small peaks very close to the noise floor, probably corresponding to other cavity modes. Additionally, a small DC bias, different for both signals, is visible.

In general, the peaks in the **PD** signals are not necessarily as pronounced as they are in Fig. 3.4, which in some cases can result in a fairly high **signal to noise ratio (SNR)**, with the peak of the weaker signal being buried in noise, as is the case for the portion of measurement shown in Fig. 3.5. In this case, the sampler **PD** peak is just above the noise floor, and normalizing the (also fairly noisy) transmission **PD** signal with that data would result in a point in the scan of poor quality.

For the sake of processing the large volume of data produced by this high resolution scan, it is useful to have some method to quantify the quality of the data in order to automatically filter out that which is of poor quality. For this purpose the statistical, or Pearson, correlation $\rho(X, Y)$ was employed. For two random variables, X and Y , it can be calculated from the covariance $\sigma(X, Y)$ between the two, normalized by the variance σ_X, σ_Y of each[39]:

$$\rho(X, Y) = \frac{\sigma(X, Y)}{\sigma_X \sigma_Y} \quad (3.1)$$

The correlation is bounded by $-1 \leq \rho \leq 1$, with -1 indicating that random variables are anti-correlated, 0 indicating no correlation, and 1 indicating perfect correlation. The two **PD** signals are not random variables, but can be treated as samples from a random distribution, from which the correlation can be estimated, as done by the **scipy** Python

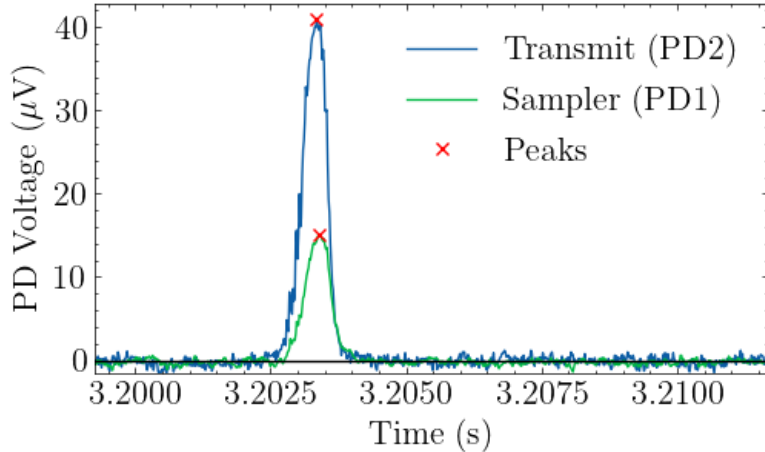


Figure 3.4: A further closeup of a clearly defined single peak, showing the Sampler PD signal closely mirroring the transmission signal in shape, only at a smaller scale. The DC offset has also been removed from the signals, and the maximum of each peak labeled. The Pearson correlation between the two signals is $\rho = 0.9028$.

package's `scipy.stats.pearsonr()`¹ method². In the case of Fig. 3.4, the calculated correlation between the transmission and sampler PD signals was $\rho = 0.9028$, while Fig. 3.5 only boasts a correlation of $\rho = 0.5473$. For this experiment, a threshold of $\rho \geq 0.9$ was found (by visual examination of various filtered and unfiltered peaks) to work well at filtering out most of the low quality peaks with poor SNR.

After rejecting all data below the correlation threshold, taking the ratio of the transmission signal to the sampler signal and associating the normalized transmission with a corresponding wavelength, the resulting spectral scan shown in Fig. 3.6 is produced. Several details are immediately obvious. First, even after filtering out data according to correlation, the constructed scan still appears remarkably noisy. Second, through the noise, there does appear to be a trend in the data which matches shape of the white light absorption. The third observation is that this trend seems to be shifted by about 0.2 nm.

Due to the low intensity of the SHG, the wavelength of the more powerful fundamental

¹[scipy.stats.pearsonr\(\) documentation](#)

²There are some caveats to estimating the Pearson correlation in this way, specifically regarding the normality of the distribution underlying the samples [40]. In practice, for this experiment it provided an adequate metric for which a threshold could be set to discard low quality data, with the quantity of available data being large enough that setting a high threshold still retained plenty of data points.

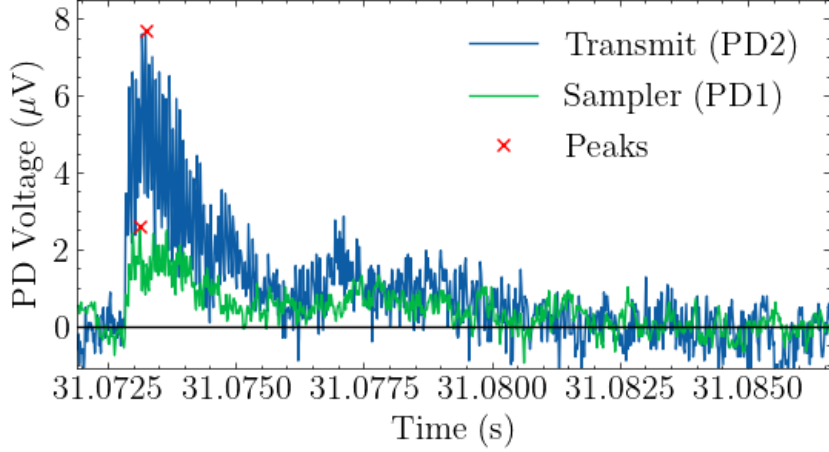


Figure 3.5: A closeup of a much noisier pair of peaks. In this case, the sampler signal is just barely above the noise floor, and the actual location of the peak is poorly defined. As a result, normalizing the height of the transmission peak, which in and of itself is somewhat noisy, with the sampler signal is suspect at best. The Pearson correlation between the two signals is only $\rho = 0.5473$.

laser frequency was monitored instead, and the **SHG** wavelength for the scan was calculated by halving the fundamental wavelength (e.g. $\lambda_{shg} = \lambda_{fundamental}/2$). This exactly half relationship was tested by measuring the wavelength of the **SHG** light using the Princeton Instruments spectrometer used for the white light transmission measurement, and a Thorlabs CSS compact spectrometer. In the case where $\lambda_{fundamental} = 1149.574\text{ nm}$ (exactly half of which is 574.784 nm), the Princeton Spectrometer measured the **SHG** light to have a peak wavelength of $\lambda_{shg} = 574.586\text{ nm}$ (Fig. 3.7a) yielding a % error of 0.034% from the theoretically expected value, while the compact spectrometer (which is much less accurate) measured a $\lambda_{shg} \approx 574.582\text{ nm}$ (somewhere between the 574.505 nm and 574.666 nm sampling wavelengths of the spectrometer, Fig. 3.7b), meaning a % error of 0.035%. Both spectrometers confirm that the **SHG** wavelength is incredibly close to the theoretically predicted wavelength, but the small percent error belies a systemic offset of $\approx 0.20\text{ nm}$, which explains the offset seen in Fig. 3.6, and can be attributed to the Angstrom Wavelength meter requiring re-calibration.

Indeed, as shown in Fig. 3.8, after applying a rolling average filter of 1000 samples, and shifting the spectral scan by 0.20 nm, the data lines up with the white light spectroscopy remarkably well, at least towards higher wavelengths.

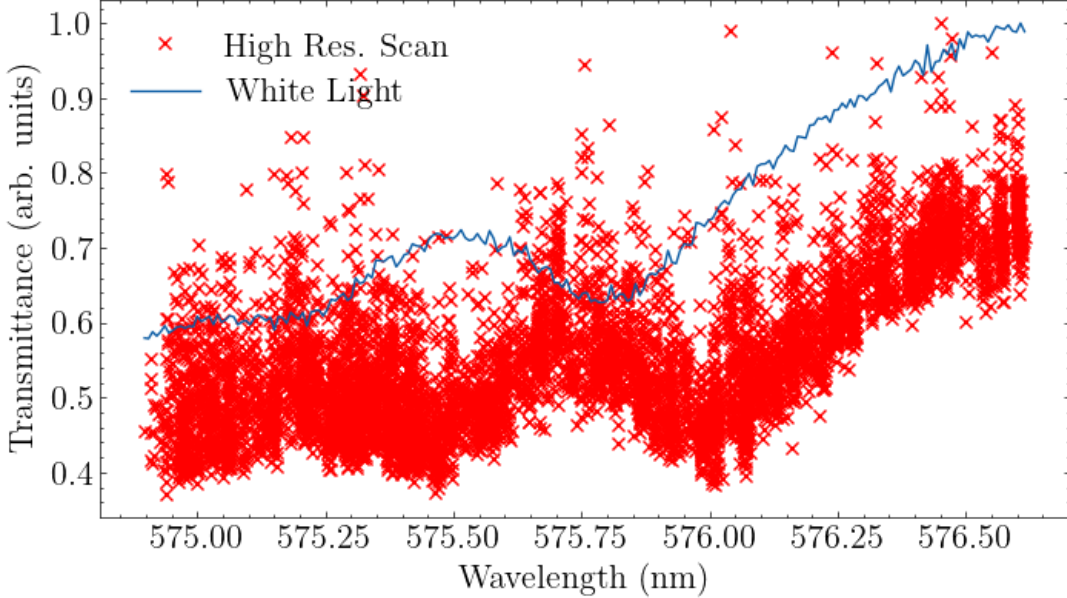


Figure 3.6: A high resolution laser light transmission scan over the range of 575 nm to 576.5 nm, constructed by normalizing the height of peaks in the transmission PD signal with the sampling PD signal, and plotting the resulting ratio as a function of wavelength. Segments of signals with $\rho < 0.9$ were rejected. The high resolution scan was also normalized with respect to any wavelength dependence of the beam sampler using measurements taken through a window in the sample holder as opposed to transmission through the sample. Also plotted is a white light transmission spectroscopy signal for comparison to the high resolution scan. Both signals have been normalized to have a maximum value of 1 for comparison.

From this point, a transformation from the Transmission-Wavelength space to the Absorption-Energy space is necessary for further analysis. Specifically, this allows for the calculation and removal of the phonon-background on which the Yellow P-exciton series rests. The phonon background, shown in Fig. 3.9 for the relevant portion of the spectrum as a green line, was calculated as the sum of Eq. 1.4 for the Γ_3^- to the yellow and green 1S excitons, Eq. 1.7 for the P-exciton continuum, and Eq. 1.9 for the Urbach tail, following [1]:

$$\alpha_{bkg} = \alpha_{1S,y}^3 + \alpha_{1S,g}^3 + \alpha_{P\text{cont}} + \alpha_{\text{Urbach}} \quad (3.2)$$

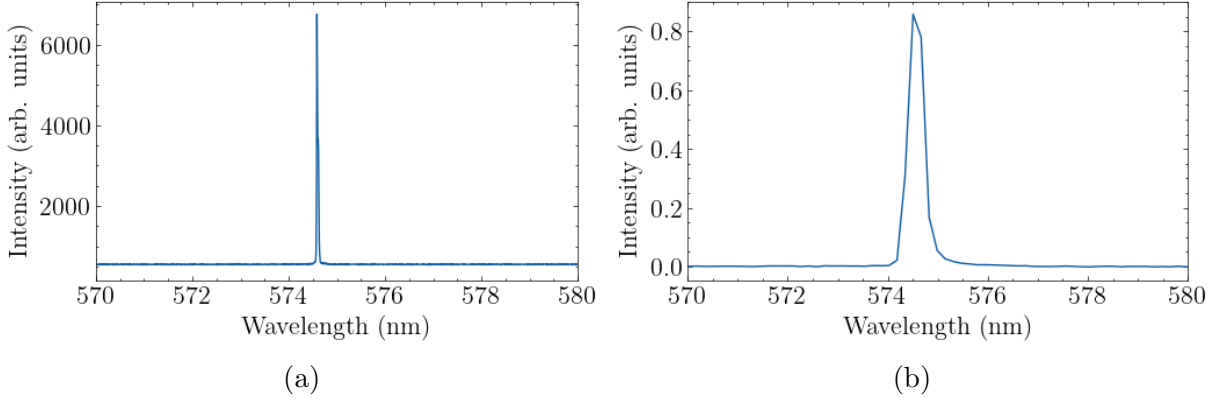


Figure 3.7: (a) The spectral response of the Princeton spectrometer to SHG light produced with a fundamental wavelength of 1149.574 nm, as measured by the Angstrom wavelength meter. The maximum of the peak occurs at 574.586 nm. (b) The spectral response of the Thorlabs CSS compact spectrometer to the same light as the Princeton spectrometer. The resolution of this small device is noticeably worse, as is to be expected of its small size. The maximum of the peak occurs between 574.505 nm and 574.666 nm.

The values used in Eq. 1.4 for the Γ_3^- to 1S yellow and 1S green exciton transitions are listed in Table 3.1.

Following background removal, the high resolution scan and white light absorption signals can be overlaid on top of and scaled to another white light spectrum measured at 100 K, reproduced using data from [2]. This data from the temperature dependent study can serve as a second basis of comparison for the high resolution scan measurement. Specifically, Eq. 1.3 can be fit to the resonance peaks in each data series, and the values of the fit parameters (E_n , C_n , Γ_n , Q_n) compared. For a description of the fitting process, see Appendix A. The results of this fitting to the $n = 4, 5$ peaks of the three signals shown in Fig. 3.10 are summarized in Table 3.2. The fit to the high resolution scan is also depicted in Fig. 3.11.

Once the E_{ns} have been extracted using Eq. 1.3, another step of fitting can be performed using Eq. 1.2 to extract values for E_g and R_y (with δ assumed to be 0). For the two white light absorption spectroscopy, values for E_n obtained by fitting all four visible peaks ($n = 2, 3, 4, 5$) were used. For the high resolution scan, two fits are considered, one with two E_n s corresponding to $n = 4, 5$ from the original scan, and one including three E_n s. In this case using three E_n s, $n = 4, 5$ are as before from the original high resolution scan, but a value of E_n for $n = 3$ is "borrowed" from the white light data, for the purpose of

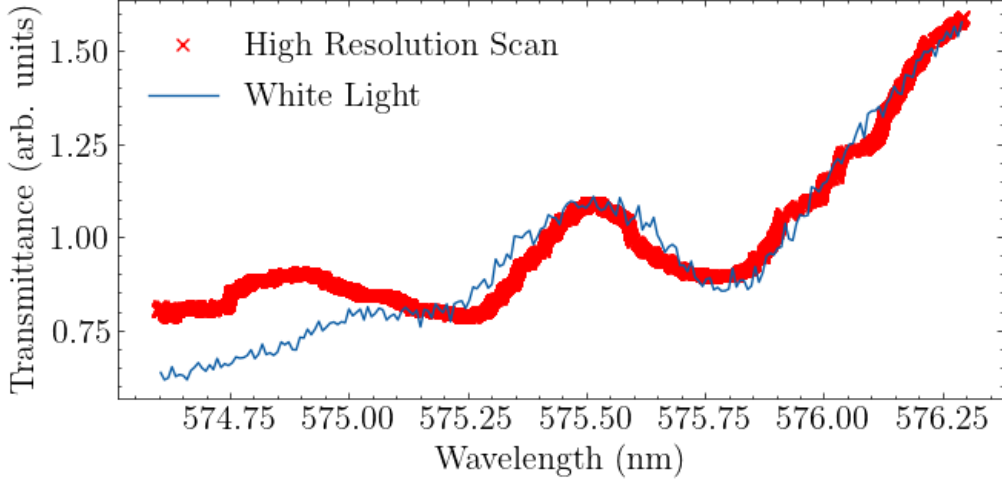


Figure 3.8: The signal from Fig. 3.6 after being filtered with a 1000 sample rolling average filter, and offset by 0.2 nm to account for the systemic error in the Angstrom wavelength meter.

having more points to fit to. The values obtained by fitting Eq. 1.1 are listed in Table 3.3. The validity and motivation for borrowing E_3 from the white light spectrum is examined further below, in the Discussion.

3.4 Discussion

The first topic bearing discussion is the remarkable amount of variance in the transmittance intensity for a given wavelength, seen in 3.6. Most likely, this is a symptom of the low power of the SHG light which introduces uncertainty in the ratio between the intensity measured by the pre and post-transmission photodetectors, even after the rejection of low correlation signals. This could be likely improved upon with a stronger light source. In the meantime, however, a rolling average filter of the signal seems adequate, as the result quite closely resembled the spectrum obtained via white light spectroscopy (Fig. 3.8), at least for these relatively small values of $n = 4, 5$ (corresponding to relatively wide/large peaks). However, such noise could make resolving peaks at larger values of n difficult, as the features are dramatically smaller, meaning that the system, as is, might be unable to resolve peaks like $n = 12$ at 4 K.

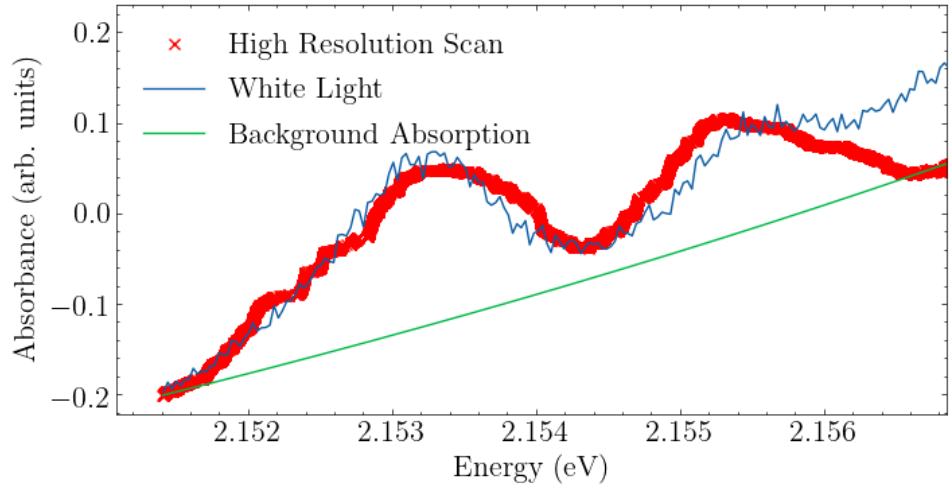


Figure 3.9: The high resolution scan and white light transmission spectra, transformed to be in terms of Energy and Absorbance. Also shown is the calculated phonon background signal.

As previously mentioned, once filtered the high resolution scan follows both the concurrently and previously taken white light spectra quite well (Figs. 3.8, 3.10), at least within the 2.152 eV to 2.156 eV range, and with some deviation at the higher energy tail. The values for E_n from Table 3.2 support the assertion that the peaks line up well at least in terms of their relative energies, as the E_n values for $n = 4$ and $n = 5$ are all quite similar. One note is that the $n = 4$ and $n = 5$ peaks appear slightly closer together in the high resolution data than they do in the white light data, a fact which is reflected in the fit values for E_n .

There are other imperfections which are clearly noticeable by visual inspection. For example, the relative heights of the $n = 4$ and $n = 5$ peaks in the high resolution scan are closer than they are in the spectra obtained by white light. As a result, even when scaled to match the white light signal, the height of the $n = 4$ peak of the high resolution data is smaller than height of the $n = 4$ white light peak, while the $n = 5$ peak of the high resolution data is larger. This may be due in part to the rolling average filter applied to the data, as a larger window seemed to worsen the effect, bringing the $n = 4$ and 5 peaks even closer to the same height.

Unfortunately, the two parameters which govern the size of the peak, the oscillator strength C_n and peak linewidth Γ_n , are unable to offer much insight, as they have values

Paramter	Value
ρ	$5.14 \times 10^3 \text{ kg/m}^3$
n_R	2.94
a_y	0.81 nm
a_b	1.72 nm
a_g	0.76 nm
$M_{1S}^{(y)}$	$2.16m_0$
$\hbar\omega_3$	13.6 meV
$ p_{78} ^2 / m_0$	2.66 eV
$D_{3;68}^{(0)}$	25.45 eV nm^{-1}
$D_{3;68}^{(2)}$	0.168 nm^2
$E_{1S}^{(y)}$	2.033 eV
$E_{1S}^{(g)}$	2.154 eV
$E_{1S}^{(b)}$	2.569 eV
$E_{2S}^{(b)}$	2.620 eV

Table 3.1: Constants listed in [1], used in Eq. 1.4 to calculate the portion of the absorption background arising from the Γ_3^- phonon to 1S yellow and green exciton transitions.

which are not entirely consistent even within the same data series. For example, for the temperature dependent data, C_n increases going from $n = 4$ to $n = 5$, while the opposite would be expected. Then for the white light data $n = 5$, the value of C_n is suddenly one order of magnitude smaller than all of the other C_n values. For Γ_n , the values going from $n = 4$ to $n = 5$ should generally grow smaller, which we see for the white light and high resolution scan data, but not for the temperature dependent study data.

Finally, examining the last of the asymmetric Lorentzian parameters, the eccentricity parameter Q_n , we find that for $n = 4$ all values are slightly negative, indicating the peak is leaning towards higher energy. Moving to $n = 5$, however, all of the values are positive, indicating a lean towards lower energy. In general, the behavior of the last resolvable peak having $Q_n > 0$ and most other peaks having $Q_n \leq 0$ was previously seen to be consistent across a number of temperatures [2].

Using the fit E_n values, estimates for E_g and R_y were also obtained via further fitting. All four values of E_g listed in Table 3.3 agree down to a difference of 1 meV, which is reassuring. The R_y column, on the other hand, is a little more interesting. Specifically, the white light absorption spectra data suggest an $R_y \approx 95 - 100$ meV. This value makes sense taking into account the temperature dependence of R_y examined in [2]. On the other hand,

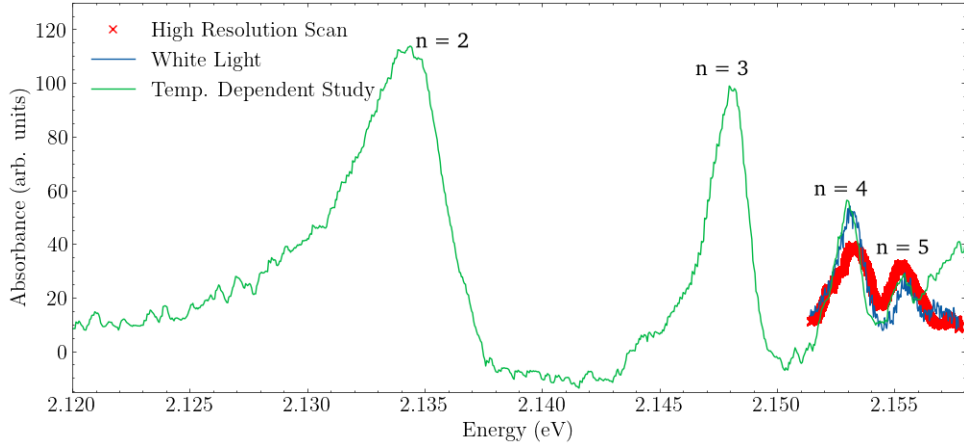


Figure 3.10: The ECDL based high resolution spectral scan and white light absorbance spectroscopy signals overlaid on top of another white light absorbance spectrum, reproduced using data from [2]. The white light and scan data have been scaled to the same scale as the reproduced data, for the sake of a direct comparison of the values obtained by fitting Eq. 1.3 to each peak.

the R_y calculated from the high resolution scan data using only the first two peaks is only 70.45 meV, which is a significant departure from typically reported values [1, 3, 15]. This value for R_y is most likely a result of trying to fit an equation with two free parameters to only two data points. Indeed, the addition of a third E_n , corresponding to $n = 3$ and borrowed from the white light spectrum fitting, brings the fit value for R_y back up to 94.25 meV, which well is within the realm of plausibility.

Evaluation of the fitting of E_n , and the validity of "borrowing" $n = 3$ for the high resolution scan E_g and R_y fitting can be further explored by examining the adherence of the fit parameters to an n -dependent scaling law. Specifically, we expect the spacing between each E_n shifted by E_g to scale with n^{-2} , since $E_g - E_n = R_y/n^2$. Fig 3.12 shows $E_g - E_n$ vs n on a log-log scale for the temperature dependent study data, the white light data taken in this experiment, and the high resolution scan data. A guideline scaling exactly as n^{-2} has been added for visual comparison. Using the values for E_n obtained from asymmetric Lorentzian fitting, together with the values from Table 3.3, $E_g - E_n = R_y/n^{(\text{power})}$ can be fit, in order to obtain an estimate for the exponent which n is raised to. Fitting the temperature dependent data yields a scaling rate of $n^{-2.10}$, fitting the white light data yields an exponent of -2.16, fitting the high resolution scan data ($n = 4, 5$) gives -1.98, and fitting the high resolution scan with $n = 3$ borrowed from the white light data yields -2.12.

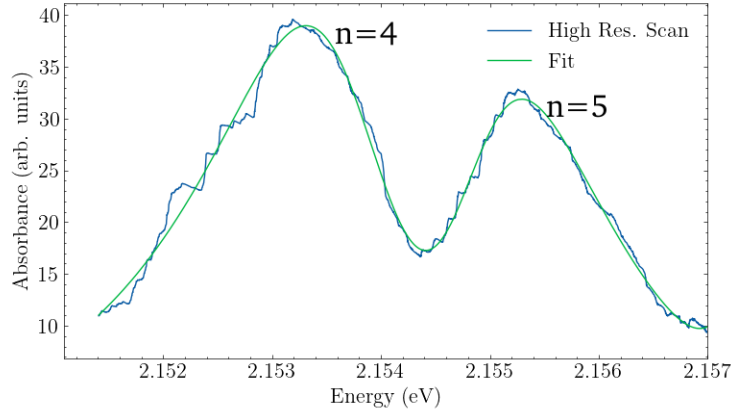


Figure 3.11: The fit line obtained when fitting a sum of asymmetric Lorentzians to the high resolution spectral scan. Only two peaks, corresponding to the $n = 4$ and $n = 5$ resonances were fit.

Interestingly, fitting the high resolution data with only two data points gives the closest exponent to the expected scaling value of n^{-2} , but this is probably due to the fact that we are using only two data points to fit a rearranged version of Eq. 1.1 with parameters previously extracted from Eq. 1.1 itself. The deviation of the other fits from a perfect n^{-2} is small, and may be explained by the relatively small number of peaks visible at 100 K. Overall, it seems that the $E_g - E_n$ scaling of the high resolution scan data is consistent with the expected scaling behavior, both by numerical comparison of the fit exponent, and by visual inspection of Fig. 3.12.

Peak	E_n (eV)	C_n (arb. units)	Q_n	Γ_n (eV)
Temperature dependent*, $n = 4$	2.1532	0.04924	-0.2921	0.001557
White light, $n = 4$	2.1532	0.03155	-0.1014	0.001328
ECDL scan, $n = 4$	2.1537	0.06675	-0.3930	0.002449
Temperature dependent*, $n = 5$	2.1554	0.0590	0.006347	0.002246
White light, $n = 5$	2.1551	0.004348	1.0000	0.001005
ECDL scan, $n = 5$	2.1548	0.02459	0.9996	0.001946

Table 3.2: Fit values for the parameters of Eq. 1.3, using three different data series. *Values are reproduced from [2] as a basis for comparison to the high resolution absorbance scan and white light absorption spectrum produced here.

Measurement	E_g (eV)	R_y (meV)
Temperature dependent*	2.159	96.75
White light	2.158	99.5
ECDL scan, $n = 4, 5$	2.158	70.45
ECDL scan [†] , $n = 3_{borrowed}, 4, 5$	2.159	94.25

Table 3.3: Values for E_g and R_y extracted by fitting Eq. 1.2 using the E_n values obtained by fitting the asymmetric Lorentzian. *Values are reproduced from [2] as a basis for comparison to the high resolution absorbance scan and white light absorption spectrum produced here. [†] In this case, a value for E_n for $n = 3$ is "borrowed" from the E_n fit to the white light data.

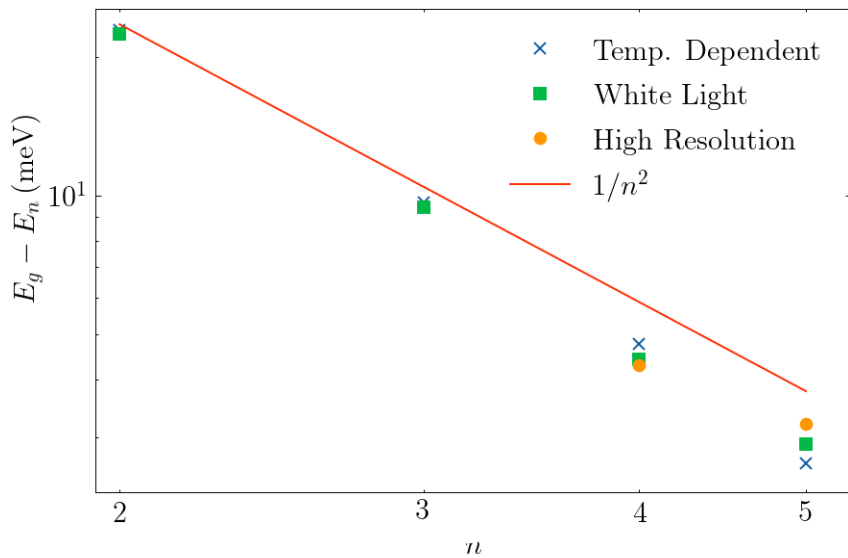


Figure 3.12: $E_g - E_n$ vs n , for each of the three data series, plotted on a log-log scale to make the exponential scaling appear linear. A guideline scaling with exactly n^{-2} is added for visual comparison, showing that the scaling of the experimental E_n s deviates from the expected scaling rate, but not significantly. Notably, the two data points from the high resolution scan are on trend with the rest of the data.

Chapter 4

Conclusion

For the purposes of exploring Rydberg exciton physics in Cu₂O, a narrow line-width tunable laser in the form of an ECDL with a bowtie cavity for enhanced SHG was designed and constructed. Theoretical background for the laser source itself, a stable wavelength reference in the form of an FP cavity, the SHG cavity, and the PDH laser stabilization method were given. The design and construction of each subsystem was detailed, and practical guides for the optical alignment of each element were provided.

At the time of its use, the system was incomplete. Namely, the laser beam was unaligned to the FP cavity due to recent changes to the optical path and therefore the FP cavity was completely un-used. In addition, the SHG cavity produced lower than expected output power and was unable to be locked to the laser's wavelength to achieve consistent resonance. Nonetheless, by sweeping the SHG cavity through resonance points, brief bursts of light were able to be used to perform a transmission spectroscopy scan over the P-exciton energies of a Cu₂O sample cooled to 100 K. A traditional white light transmission spectroscopy measurement was also made using a spectrometer for the sake of comparison.

Following the experiment, the laser light transmission data was analyzed, and used to reconstruct a high resolution spectral scan. Following removal of the phonon background absorbance from the calculated absorbance signal, Toyozawa's asymmetric Lorentzian function [14] was fit to the resulting clearly visible resonance peaks, allowing for the extraction of a number of descriptive parameters. Further analysis was then performed, using the extracted values of the energy of each resonance peak, E_n , to calculate values for the band gap energy E_g and the Rydberg energy R_y . Lastly, the fit values for E_g and R_y were then used to perform an analysis of the scaling of the quantity $E_g - E_n$, which was compared to the expected scaling rate of n^{-2} .

4.1 Reflections

The yellow P-exciton spectrum obtained by the high resolution laser transmission scan was shown to agree well with both the concurrently taken white light transmission spectrum and a spectrum produced using the same method, reproduced using data from a previous study [2]. Particularly, the energy location of each peak E_n at a given n was consistent across all three sets of data. Further analysis was then performed by fitting to Eq. 1.1 to extract the bandgap E_g and Rydberg R_y energies. E_g was seen to be incredibly consistent across all data, although the value of R_y fit from the high resolution scan was significantly off trend, a fact which is attributed to the presence of only 2 data points from the high resolution scan in this particular fitting. The scaling of the difference between the band gap energy and each peak location, $E_g - E_n$, was also examined. All three sets of data were found to have an exponential scaling as a function of n close to the predicted value of n^{-2} . The values for the asymmetry parameter, Q_n , were also consistent across the data.

The results of fitting other parameters were less conclusive, however. By visual inspection of Fig. 3.10 it is clear to see that the relative heights of the $n = 4$ and 5 peaks of the high resolution scan data are closer than they should be, in comparison to the same peaks in both of the data series obtained by white light spectroscopy. Unfortunately, the resonance peak parameters corresponding to the shape of the peak, C_n and Γ_n , were the least consistent across all of the data series, and thus offered no particular insight into this phenomenon.

The analysis of the high resolution scan was limited by the fact that only two peaks were scanned. In addition, the two peaks whose absorbance spectrum were reproduced in this way were the highest visible peaks at the temperature at which the experiment was conducted. The highest n visible peaks at a given temperature are the peaks that consistently fit poorly, with parameters frequently off-trend as seen in [2]. Performing the same study at lower temperatures would allow for many peaks to be scanned, fixing the above issues and allowing for a fuller comparison with spectra obtained by broadband white light transmission spectroscopy. In addition, the inclusion of many more peaks would enable the meaningful evaluation of the scaling laws of parameters other than E_n , as was performed in [2].

4.2 Practical lessons

Reflecting upon difficulties faced throughout the course of this project, there are many practical lessons to be learned. First, although a Littrow configuration was chosen for this project in part due to the higher power output than a Littman-Metcalf configuration [26, 29], the need to couple the output to a fiber to provide a fixed source for the rest of the optical elements resulted in an immediate power loss of around 50% due to coupling losses. Thus, the fixed output of a simple Littman-Metcalf configuration **ECDL** may be able to result in more power delivered to the **SHG** cavity overall, with more advanced designs helping to overcome the Littman-Metcalf efficiency shortcoming possibly leading to further increases in power [41].

Reflections regarding the **SHG** cavity itself include the recommendation to use smaller (25 mm instead of 50 mm) mirrors in the construction of the bowtie cavity to avoid the issue of the beam clipping on the cavity itself, and make it easier to collimate the output light by providing more room for collimation lens positioning. The locking issues experienced with the **SHG** cavity are thought to be due to the Moku Lab having an insufficient output voltage range to cover the **FSR** of the cavity.

Lastly, considerable difficulty was encountered when adjusting the length of the **FP** cavity by rotating the inner ring of the brass cap. Lubrication was not applied to the threads between the rings of the cap, which ended up causing an issue when trying to rotate the ring after it having been left in the same position for some time, because the brass had oxidized in place. Thus, when a standard optical wrench was applied to rotate the inner ring, considerable force was required, which eventually caused the brass slots for the wrench teeth to chip, which in turn, got caught in the threads, and locked the entire inner part of the cap up. This required considerable force to work lose and time to clean the threads. Lubricating the joint from the start would probably prevent the issue, but it may also be prudent to machine deeper slots (to prevent the same sort of chipping that occurred on the shallow slots) for a different wrench further from the threads, so that any chips which do form do not immediately get caught in said threads.

4.3 Fulfilment of Objectives

Overall, the stated objective of completing a narrow linewidth tunable laser system for use in a high resolution scan to resolve yellow P-exciton peaks unreasonable due to resolution limits of traditional spectrographic techniques was not achieved. First, the laser system

itself is incomplete. The **FP** cavity was unaligned, and therefore un-characterized and unused. The **SHG** cavity was unable to be locked to a resonance point for any significant time scale, and the conversion efficiency was much lower than what is theoretically predicted. Lastly, the laser system was not used to scan any previously unsolvable peaks.

Although the laser system is not complete, it was shown that even in its current state, it is able to be utilized to perform a high resolution scan that mirrors the expected/observed spectral features revealed by white light spectroscopy. Specifically, the scan was processed in the same manner as a white light spectrum, including phonon background removal, and fitting by an asymmetric Lorentzian function in order to extract and compare qualitative parameters. This serves as motivation for further experiments using the same technique demonstrated in this pilot experiment at lower temperatures.

4.4 Future Prospects

Several challenges remain to declare the laser system fully operational, but completion will present the opportunity for many exciting experiments, the first of which is high resolution spectroscopy of high n resonance peaks in the yellow P-exciton series at low temperatures. Such a spectral scanning experiment can advance the field by including an analysis of the quantum defect, enabled by resolving many resonance peaks [15], and can be further extended by the addition of an electric field applied to the sample, as described in [12].

From there, a second laser (perhaps based on **sum frequency generation (SFG)** [42, 43] instead of **SHG**) would open the door for a whole new class of experiments, including pump/probe measurements and prospects like electromagnetically induced transparency [17, 44] and further exploration of the Rydberg blockade in Rydberg excitons, [16, 17]. A full understanding of the Rydberg blockade may then facilitate the realization of a two qubit gate as it did in the neutral atom space [9, 10, 11], which further opens the door for the implementation of a solid state quantum information processing platform.

References

- [1] Florian Schöne, Heinrich Stoltz, and Nobuko Naka. Phonon-assisted absorption of excitons in Cu₂O. *Phys. Rev. B*, 96:115207, Sep 2017.
- [2] Dongyeon Daniel Kang, Aaron Gross, HeeBong Yang, Yusuke Morita, Kyung Soo Choi, Kosuke Yoshioka, and Na Young Kim. Temperature study of rydberg exciton optical properties in Cu₂O. *Phys. Rev. B*, 103:205203, May 2021.
- [3] T Kazimierczuk, D. Fröhlich, S Scheel, H Stoltz, and M Bayer. Giant Rydberg excitons in the copper oxide cu₂O. *Nature*, 514(7522):343–347, oct 2014.
- [4] National Academies of Sciences, Engineering, and Medicine. *Quantum Computing: Progress and Prospects*. National Academies Press, Washington, D.C., March 2019. Pages: 25196.
- [5] Loic Henriet, Lucas Beguin, Adrien Signoles, Thierry Lahaye, Antoine Browaeys, Georges-Olivier Reymond, and Christophe Jurczak. Quantum computing with neutral atoms. *Quantum*, 4:327, September 2020. arXiv: 2006.12326.
- [6] Masakazu Hayashi. Absorption Spectrum of Cuprous Oxide in the Visible Region. *J. of the Faculty of Science, Hokkaido University, Japan, Ser. II*, 4(2):343–347, 1952.
- [7] Masakazu Hayashi and Kiichiro Katsuki. Hydrogen-Like Absorption Spectrum of Cuprous Oxide. *J. Phys. Soc. Jpn*, 7(6):599–603, nov 1952.
- [8] E. F. Gross. Optical spectrum of excitons in the crystal lattice. *Il Nuovo Cimento*, 3(S4):672–701, April 1956.
- [9] Daniel Tiarks, Steffen Schmidt-Eberle, Thomas Stoltz, Gerhard Rempe, and Stephan Dürr. A photon–photon quantum gate based on Rydberg interactions. *Nature Physics*, 15(2):124–126, February 2019. Bandiera_abtest: a Cg_type: Nature Research Journals Number: 2 Primary_atype: Research Publisher: Nature Publishing

Group Subject_term: Atomic and molecular interactions with photons;Quantum information;Quantum optics;Qubits Subject_term_id: atomic-and-molecular-interactions-with-photons;quantum-information;quantum-optics;qubits.

- [10] T. M. Graham, M. Kwon, B. Grinkemeyer, Z. Marra, X. Jiang, M. T. Lichtman, Y. Sun, M. Ebert, and M. Saffman. Rydberg-Mediated Entanglement in a Two-Dimensional Neutral Atom Qubit Array. *Physical Review Letters*, 123(23):230501, December 2019. Publisher: American Physical Society.
- [11] M. D. Lukin, M. Fleischhauer, R. Cote, L. M. Duan, D. Jaksch, J. I. Cirac, and P. Zoller. Dipole Blockade and Quantum Information Processing in Mesoscopic Atomic Ensembles. *Physical Review Letters*, 87(3):037901, June 2001. Publisher: American Physical Society.
- [12] J. Heckötter, M. Freitag, D. Fröhlich, M. Aßmann, M. Bayer, M. A. Semina, and M. M. Glazov. High-resolution study of the yellow excitons in Cu₂O subject to an electric field. *Physical Review B*, 95(3):035210, January 2017.
- [13] J. Heckötter, D. Janas, R. Schwartz, M. Aßmann, and M. Bayer. Experimental limitation in extending the exciton series in Cu₂O towards higher principal quantum numbers. *Phys. Rev. B*, 101:235207, Jun 2020.
- [14] Yutaka Toyozawa. Theory of Line-Shapes of the Exciton Absorption Bands. *Prog. Theor. Phys.*, 20(1):53–81, 07 1958.
- [15] Florian Schöne, Sjard-Ole Krüger, Peter Grünwald, Marc Aßmann, Julian Heckötter, Johannes Thewes, Heinrich Stolz, Dietmar Fröhlich, Manfred Bayer, and Stefan Scheel. Coupled valence band dispersions and the quantum defect of excitons in Cu₂O. *Journal of Physics B: Atomic, Molecular and Optical Physics*, 49(13):134003, June 2016. Publisher: IOP Publishing.
- [16] Julian Heckötter, Valentin Walther, Stefan Scheel, Manfred Bayer, Thomas Pohl, and Marc Aßmann. Asymmetric Rydberg blockade of giant excitons in Cuprous Oxide. *arXiv:2010.15459 [cond-mat]*, October 2020. arXiv: 2010.15459.
- [17] V. Walther, P. Grünwald, and T. Pohl. Controlling Exciton-Phonon Interactions via Electromagnetically Induced Transparency. *Physical Review Letters*, 125(17):173601, October 2020. Publisher: American Physical Society.

- [18] G. M. Kavoulakis, Yia-Chung Chang, and Gordon Baym. Fine structure of excitons in Cu₂O. *Physical Review B*, 55(12):7593–7599, March 1997. Publisher: American Physical Society.
- [19] Dominik Christiansen, Malte Selig, Gunnar Berghäuser, Robert Schmidt, Iris Niehues, Robert Schneider, Ashish Arora, Steffen Michaelis de Vasconcellos, Rudolf Bratschitsch, Ermin Malic, and Andreas Knorr. Phonon Sidebands in Monolayer Transition Metal Dichalcogenides. *Physical Review Letters*, 119(18):187402, November 2017. Publisher: American Physical Society.
- [20] Franz Urbach. The Long-Wavelength Edge of Photographic Sensitivity and of the Electronic Absorption of Solids. *Physical Review*, 92(5):1324–1324, December 1953. Publisher: American Physical Society.
- [21] Hyeran Kong. Towards many-body physics with Rydberg-dressed cavity polaritons. Master’s thesis, University of Waterloo, May 2018.
- [22] John F Barry. *Laser cooling and slowing of a diatomic molecule*. PhD thesis, Yale University, December 2013.
- [23] Clifton Fonstad. *Lecture 20: Laser Diodes*. Lecture notes in Compund Semiconductors. MIT Open Courseware, 2003.
- [24] Wenbo Wang, Arkady Major, and Jitendra Paliwal. Grating Stabilized External Cavity Diode Lasers for Raman Spectroscopy – A Review. *Applied Spectroscopy Reviews*, 47, February 2012.
- [25] Michael G. Littman. Single-mode operation of grazing-incidence pulsed dye laser. *Optics Letters*, 3(4):138–140, October 1978. Publisher: Optical Society of America.
- [26] Wenxian Hong. Design and Characterization of a Littrow Configuration External Cavity Diode Laser.
- [27] Richardson Gratings. Technical Note 11 - Determination of the Blaze Wavelength, September 2012.
- [28] Stephanie E. White and Maria Ana Cataluna. Unlocking Spectral Versatility from Broadly-Tunable Quantum-Dot Lasers. *Photonics*, 2(2):719–744, June 2015. Number: 2 Publisher: Multidisciplinary Digital Publishing Institute.

- [29] Michael G. Littman and Harold J. Metcalf. Spectrally narrow pulsed dye laser without beam expander. *Applied Optics*, 17(14):2224–2227, July 1978. Publisher: Optical Society of America.
- [30] I. Shoshan, N. N. Danon, and U. P. Oppenheim. Narrowband operation of a pulsed dye laser without intracavity beam expansion. *Journal of Applied Physics*, 48(11):4495–4497, November 1977. Publisher: American Institute of Physics.
- [31] Haiyin Sun. Simplification of laser diode astigmatism measurement. *Optical Engineering*, 50(10):104202, October 2011. Publisher: International Society for Optics and Photonics.
- [32] Eric D. Black. An introduction to Pound–Drever–Hall laser frequency stabilization. *American Journal of Physics*, 69(1):79–87, December 2000. Publisher: American Association of Physics Teachers.
- [33] Norman Hodgson and Horst Weber. *Optical Resonators*. Springer-Verlag London, 1997.
- [34] Jae-Sang Park and Ji-Hwan Kim. Coefficients of thermal expansion for single crystal piezoelectric fiber composites. *Composites Part B: Engineering*, 38(7):795–799, October 2007.
- [35] Atsushi Yamaguchi. *Metastable State of Ultracold and Quantum Degenerate Ytterbium Atoms: High-Resolution Spectroscopy and Cold Collisions*. PhD thesis, Kyoto University, March 2008.
- [36] Robert Eckardt, Hisashi Masuda, Yuan Xuan Fan, and Robert Byer. Absolute and relative nonlinear optical coefficients of KDP, KD*P, BaB₂O₄, LiIO₃, MgO:LiNbO₃, and KTP measured by phase-matched second harmonic generation. *IEEE Journal of Quantum Electronics*, 26(5), May 1990.
- [37] G. D. Boyd and D. A. Kleinman. Parametric Interaction of Focused Gaussian Light Beams. *Journal of Applied Physics*, 39(8):3597–3639, July 1968. Publisher: American Institute of Physics.
- [38] Liquid Instruments. PDH Technique with Moku:Lab’s Laser Lock Box, November 2020.
- [39] Eric W. Weisstein. Statistical Correlation. Publisher: Wolfram Research, Inc.

- [40] Charles J. Kowalski. On the Effects of Non-Normality on the Distribution of the Sample Product-Moment Correlation Coefficient. *Applied Statistics*, 21(1):1, 1972.
- [41] S. Stry, S. Thelen, J. Sacher, D. Halmér, P. Hering, and M. Mürtz. Widely tunable diffraction limited 1000 mW external cavity diode laser in Littman/Metcalf configuration for cavity ring-down spectroscopy. *Applied Physics B*, 85(2-3):365–374, November 2006.
- [42] W. P. Risk and W. J. Kozlovsky. Efficient generation of blue light by doubly resonant sum-frequency mixing in a monolithic KTP resonator. *Optics Letters*, 17(10):707–709, May 1992. Publisher: Optical Society of America.
- [43] Hugo Kerdoncuff, Jesper B. Christensen, Túlio B. Brasil, Valeriy A. Novikov, Eugene S. Polzik, Jan Hald, and Mikael Lassen. Cavity-enhanced sum-frequency generation of blue light with near-unity conversion efficiency. *Optics Express*, 28(3):3975, February 2020. arXiv: 2002.05491.
- [44] David Ziemkiewicz and Sylwia Zielińska Raczyńska. Electromagnetically Induced Transparency in Media with Rydberg Excitons 2: Cross-Kerr Modulation. *Entropy*, 22(2):160, February 2020. Number: 2 Publisher: Multidisciplinary Digital Publishing Institute.
- [45] Michel Goossens, Frank Mittelbach, and Alexander Samarin. *The L^AT_EX Companion*. Addison-Wesley, Reading, Massachusetts, 1994.
- [46] Donald Knuth. *The T_EXbook*. Addison-Wesley, Reading, Massachusetts, 1986.
- [47] Leslie Lamport. *L^AT_EX — A Document Preparation System*. Addison-Wesley, Reading, Massachusetts, second edition, 1994.
- [48] Alexandros Georgakopoulos, Ariel Sommer, and Jonathan Simon. Theory of Interacting Cavity Rydberg Polaritons. *arXiv:1805.07315 [cond-mat]*, May 2018. arXiv: 1805.07315.
- [49] Logan W. Clark, Nathan Schine, Claire Baum, Ningyuan Jia, and Jonathan Simon. Observation of Laughlin states made of light. *arXiv:1907.05872 [cond-mat, physics:physics, physics:quant-ph]*, July 2019. arXiv: 1907.05872.
- [50] Logan W. Clark, Ningyuan Jia, Nathan Schine, Claire Baum, Alexandros Georgakopoulos, and Jonathan Simon. Interacting Floquet polaritons. *Nature*, 571(7766):532–536, July 2019.

- [51] Tomoki Ozawa, Hannah M. Price, Alberto Amo, Nathan Goldman, Mohammad Hafezi, Ling Lu, Mikael Rechtsman, David Schuster, Jonathan Simon, Oded Zilberg, and Iacopo Carusotto. Topological Photonics. *Reviews of Modern Physics*, 91(1):015006, March 2019. arXiv: 1802.04173.
- [52] Nathan Schine, Michelle Chalupnik, Tankut Can, Andrey Gromov, and Jonathan Simon. Electromagnetic and gravitational responses of photonic Landau levels. *Nature*, 565(7738):173–179, January 2019.
- [53] Mitsuyoshi Takahata and Nobuko Naka. Photoluminescence properties of the entire excitonic series in Cu₂O. *Physical Review B*, 98(19):195205, November 2018.
- [54] A Jolk and C Klingshirn. Linear and Nonlinear Excitonic Absorption and Photoluminescence Spectra in Cu₂O: Line Shape Analysis and Exciton Drift, 1998.
- [55] R. J. Elliott. Intensity of optical absorption by excitons. *Phys. Rev.*, 108:1384–1389, Dec 1957.
- [56] J.B. Grun, M. Sieskind, and S. Nikitine. Etude spectrophotometrique des spectres continus de Cu₂O à diverses températures. *J. Phys. Chem. Solids.*, 19(3):189–197, 1961.
- [57] M. Saffman, T. G. Walker, and K. Mølmer. Quantum information with Rydberg atoms. *Reviews of Modern Physics*, 82(3):2313–2363, August 2010. Publisher: American Physical Society.
- [58] Carl E Wieman and Leo Hollberg. Using diode lasers for atomic physics. *Rev. Sci. Instrum.*, 62(1):20, 1991.
- [59] L. Ricci, M. Weidmüller, T. Esslinger, A. Hemmerich, C. Zimmermann, V. Vuletic, W. König, and T.W. Hänsch. A compact grating-stabilized diode laser system for atomic physics. *Optics Communications*, 117(5-6):541–549, June 1995.
- [60] K B MacAdam. A narrow-band tunable diode laser system with grating feedback, and a saturated absorption spectrometer for Cs and Rb. *Am. J. Phys.*, 60(12):14, 1992.
- [61] Stephen A. Lynch, Chris Hodges, Soumen Mandal, Wolfgang Langbein, Ravi P. Singh, Liam A. P. Gallagher, Jon D. Pritchett, Danielle Pizzey, Joshua P. Rogers, Charles S. Adams, and Matthew P. A. Jones. Rydberg Excitons in Synthetic Cuprous Oxide (Cu₂O). *arXiv:2010.11117 [cond-mat, physics:physics]*, October 2020. arXiv: 2010.11117.

APPENDICES

Appendix A

Fitting Toyozawa's Formula to the Yellow and Green Exciton Spectrum

In this appendix, I describe the process of fitting Toyozawa's asymmetric Lorentzian formula[14], reproduced as Eq. 1.3, to the P-exciton series in Cu₂O. This particular discussion details for the fitting of both the yellow and green P-excitons in Cu₂O, the latter of which are not encountered in the experiment described in this thesis. I include them here simply for the sake of completely describing the difficulties I encountered in fitting Eq. A.2 to the Cu₂O P-exciton resonances I have experiences with, and because the lower number of visible peaks can serve to make for more illustrative and less busy examples of the fitting process than the yellow exciton series.

A.1 Background Removal

The green and yellow P-exciton spectra in the raw absorbance data ride atop a broad background spectrum, arising from various phonon-assisted absorption mechanisms. For the most part, this background is well described by theory [55, 56, 1], and can be calculated and removed from the absorption signal, as shown in Appendix A of [2]. This background subtraction process yields a flat yellow exciton spectrum. However, a portion of the background in the region of the green exciton peaks is not fully understood, and thus causes the green spectrum to gradually trend upward moving towards higher energy, even after background removal. Practically, this additional background was accounted for during fitting, and is described in more detail below.

A.2 Fitting Multiple Peaks

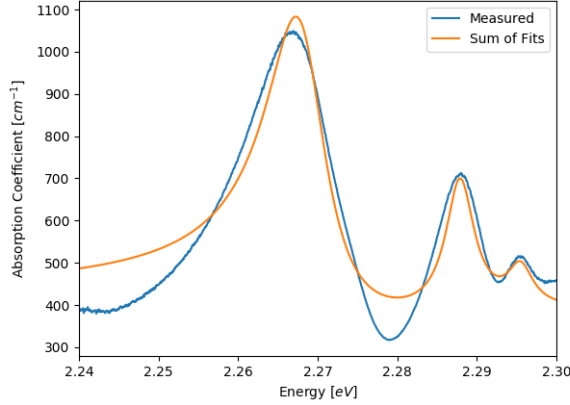


Figure A.1: An example of an attempt to fit the asymmetric Lorentzian to the resonance peaks one at a time. Generally, the quality of the fitting is bad, specifically in the valleys between peaks. Reproduced absorption spectra data of the green exciton at 4K using data from [2]

The initial attempt at fitting involved using the `curve_fit()` function in the `scipy.optimize` python package, which takes a function with k parameters, and attempts to find values for those parameters to fit the function to an array of data, to fit each of the n peaks one at a time and sum each of the fits together to reconstruct the signal. This meant that `curve_fit()` was being used to fit a total of four parameters (C_n, Γ_n, Q_n, E_n) at one time.

As can be seen in Fig. A.1, the result of this one at a time fit attempt poorly followed the original spectrum. This poor fitting performance is attributed to the fact that fitting each peak in isolation struggles when the peaks are close enough that the Lorentzian tails bleed into neighboring peaks.

The solution to this problem was to fit all peaks simultaneously. In practice, this was done by constructing a variadic function (a function with a variable number of parameters) that was a sum of $n - 1$ asymmetric Lorentzians (Eq. 1.3):

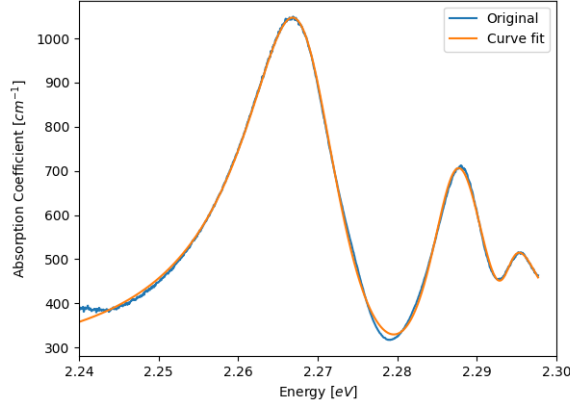


Figure A.2: The same 4 K green exciton spectra, this time with all peaks being fit simultaneously using a superposition of asymmetric Lorentzian functions. Although the quality of the fit looks much better visually, the values of the extracted physical parameters are nonsensical. Reproduced using data from [2]

$$\alpha(E) = \sum_{i=2}^n C_i \frac{\frac{\Gamma_i}{2} + 2Q_i (E - E_i)}{\left(\frac{\Gamma_i}{2}\right)^2 + (E - E_i)^2}, \quad (\text{A.1})$$

Equation A.1 was passed to `curve_fit()` to find the values of each parameter. This worked well, and produced a fit line which closely followed the original data for spectra with just a few n , such as the Green spectra at 4 K shown in Fig. A.2.

However, this method had two problems. First, for spectra with more than 5 peaks, `curve_fit()` was unable to converge, resulting in a fit that did not follow the original data at all. Second, even for the spectra shown in Fig. A.2, the values for each parameter were outside a range which made physical sense. The conclusion was that when fitting all peaks simultaneously (which means fitting $4(n - 1)$ parameters simultaneously) there were too many free parameters, resulting in either a lack of convergence or over fitting.

A.3 Fitting Constraints

The solution to the issues caused by having too many free parameters was to provide a set of reasonable guesses for the initial value of each parameter, helping the fitting to

converge, and to introduce constraints on the values the parameters could take, preventing over-fitting. For example, initial values for E_n specified roughly where each peak was centered, which could be refined to be more accurate via the fitting. For parameters like C_n , for which it was difficult to find a reasonable estimate for all values based on the individual peak fitting, a value for the largest ($n = 2$) peak was specified, and then guesses for subsequent peaks were generated based on the expected scaling laws for that parameter. In practice, the true values for these parameters deviate from the expected scaling laws at high n (< 8) due to a number of factors, but this method provided initial guesses which still yielded reasonable results. Upper and lower boundaries were also placed on the parameters to help prevent over-fitting. In practice, once the boundaries were and initial value guesses were implemented, the values of the fitting parameters rarely ran into the set boundaries, meaning that the values were not being artificially limited to what they were expected to be.

Unfortunately, some of these initial parameter values (e.g. E_n) had to be hard coded for each temperature of both the yellow and green spectra. This was done using a configuration file so that the code performing the fitting could be generic over both the yellow and green excitons across all temperatures, thanks to the variadic nature of the fitting function.

A.4 Residual Background and Fitting Boundaries

As mentioned above, the removal of the background in the green excitonic series is incomplete, and some residual background still remains. Over a small energy region, the background appears linear and increases with energy. In an attempt to accommodate the residual background during the fitting, three terms were cumulatively added to A.1 and their performance was compared. Specifically, first a term that was constant with respect to energy was added, then, while retaining the constant term, a term that was linear with respect to energy was added, and culminating in a term that was quadratic with respect to energy.

Despite the linear appearance of the background, the all three terms yielded comparable, high quality fits. As a result, for the sake of simplicity and to avoid over fitting (as additional polynomials allow for the approximation of arbitrary functions), only the constant term was used in the final fitting results.

One other fitting consideration affected by the residual background in the green excitons was the choice of energy range over which the fitting of the absorption spectrum was preformed. In the green exciton spectrum, the $n = 4$ peak (when visible), has a deep dip

into the background signal on the higher energy tail, the inclusion of which made fitting of this peak consistently poor. As a result, the upper end of the fitting boundaries for the green exciton data was chosen to exclude this tail, and only capture the downward slope of the higher energy side of the peak. In the yellow exciton spectrum, the data was similarly constrained on the upper energy end, but for a different reason. At low temperatures (i.e. ≤ 30 K), the highest n visible peak is often very close in scale to the noise in the signal. Thus, the fitting data must be carefully restricted to exclude any noise-based fluctuations in the higher energy portion of the highest peak which could confuse the fitting of the tail of the peak.

A.5 Fitting the Final Peak

Under certain circumstances, the fitting of the highest visible peak of the yellow and green exciton series proved challenging. For the yellow exciton, the challenge occurred at low (again, ≤ 30 K) temperatures, and concerned the $n = 10, 11$. peaks. The challenge with fitting this peak was predominantly caused by two factors, the first of which was the relative size of the peak compared to the background noise of the signal, as mentioned previously. The second was the resolution of the signal, as determined by the resolution of the spectrometer used in measurement.

Conversely, for the green exciton, the difficulty in fitting the higher n peak, in this case always $n = 4$, occurred at higher temperatures (≥ 70 K), and was caused by the thermal broadening of the $n = 3, 4$ peaks creating a significant overlap, as seen in Fig. A.3.

A.6 Other Fitting Attempts

Several other fitting methodologies were employed, to varying degrees of success. First, a fit using a skew Gaussian (as opposed to an asymmetric Lorentzian) was attempted, defined as:

$$f_n(E) = 2c_n \phi\left(\frac{E - E_n}{\sigma}\right) \Phi\left(\alpha \frac{E - E_n}{\sigma}\right) \quad (\text{A.2})$$

which includes an amplitude term C_n , an asymmetry term α , width in the form of a standard deviation σ , an offset centering the peak at E_n , a standard normal distribution:

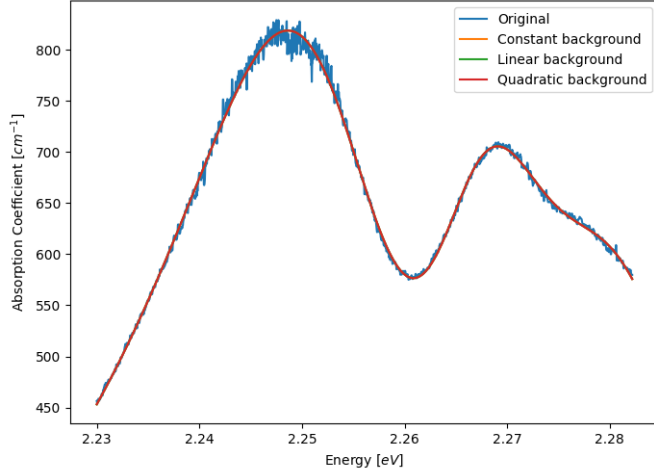


Figure A.3: An example of the Green exciton series at 70 K. The $n = 3$ and $n = 4$ peaks are beginning to overlap significantly due to thermal broadening effects, which makes fitting each peak individually difficult. Reproduced using data from [2].

$$\phi\left(\frac{E - E_n}{\sigma}\right) = \frac{1}{\sqrt{2\pi\sigma^2}} e^{-\frac{1}{2}\left(\frac{E - E_n}{\sigma}\right)^2} \quad (\text{A.3})$$

and a corresponding [cumulative distribution function \(CDF\)](#) for the normal distribution:

$$\Phi\left(\alpha \frac{E - E_n}{\sigma}\right) = \int_{-\infty}^{\left(\alpha \frac{E - E_n}{\sigma}\right)} \phi(t) dt = \frac{1}{2} \left(1 + \text{erf}\left(\alpha \frac{E - E_n}{\sqrt{2}\sigma}\right)\right) \quad (\text{A.4})$$

This function ended up fitting poorly in comparison to the Toyozawa formula, mainly in that it did not conform as well to the shape of the curve as an asymmetric Lorentzian, despite having the same number of free fitting parameters.

Another strategy that was employed was fitting the analytical first and second derivatives of A.1 to the numerical derivatives of the data. Despite the tendency of numerical differentiation to amplify the noise in the data, the first derivative fitting actually worked fairly well, although it did not produce results that were significantly better than the fitting of the original signal. The second derivative fitting proved less successful, and `curve_fit()` frequently missed an entire peak in the fitting of the data.